

# **SANDIA REPORT**

SAND2009-5968

Unlimited Release

Printed September 2009

## **Material Compatibility and Thermal Aging of Thermoelectric materials**

Nancy Yang, Scott Whalen, Alfredo Morales, Jeff Chames,  
Andrew Gardea, W. Miles Clift, and Ryan Nishimoto

Prepared by  
Sandia National Laboratories  
Albuquerque, New Mexico 87185 and Livermore, California 94550

Sandia is a multiprogram laboratory operated by Sandia Corporation,  
a Lockheed Martin Company, for the United States Department of Energy's  
National Nuclear Security Administration under Contract DE-AC04-94AL85000.

Approved for public release; further dissemination unlimited.



Issued by Sandia National Laboratories, operated for the United States Department of Energy by Sandia Corporation.

**NOTICE:** This report was prepared as an account of work sponsored by an agency of the United States Government. Neither the United States Government, nor any agency thereof, nor any of their employees, nor any of their contractors, subcontractors, or their employees, make any warranty, express or implied, or assume any legal liability or responsibility for the accuracy, completeness, or usefulness of any information, apparatus, product, or process disclosed, or represent that its use would not infringe privately owned rights. Reference herein to any specific commercial product, process, or service by trade name, trademark, manufacturer, or otherwise, does not necessarily constitute or imply its endorsement, recommendation, or favoring by the United States Government, any agency thereof, or any of their contractors or subcontractors. The views and opinions expressed herein do not necessarily state or reflect those of the United States Government, any agency thereof, or any of their contractors.

Printed in the United States of America. This report has been reproduced directly from the best available copy.

Available to DOE and DOE contractors from  
U.S. Department of Energy  
Office of Scientific and Technical Information  
P.O. Box 62  
Oak Ridge, TN 37831

Telephone: (865) 576-8401  
Facsimile: (865) 576-5728  
E-Mail: [reports@adonis.osti.gov](mailto:reports@adonis.osti.gov)  
Online ordering: <http://www.osti.gov/bridge>

Available to the public from  
U.S. Department of Commerce  
National Technical Information Service  
5285 Port Royal Rd.  
Springfield, VA 22161

Telephone: (800) 553-6847  
Facsimile: (703) 605-6900  
E-Mail: [orders@ntis.fedworld.gov](mailto:orders@ntis.fedworld.gov)  
Online order: <http://www.ntis.gov/help/ordermethods.asp?loc=7-4-0#online>



# Material Compatibility and Thermal Aging of Thermoelectric Materials

Nancy Yang, Scott Whalen, Alfredo Morales, Jeff Chames,  
Andrew Gardea, W. Miles Clift, and Ryan Nishimoto  
Sandia National Laboratories  
P.O. Box 969  
Livermore, CA. 94551-0969

## Abstract

In order to design a thermoelectric (TE) module suitable for long-term elevated temperature use, the Department 8651 has conducted parametric experiments to study material compatibility and thermal aging of TE materials. In addition, a comprehensive material characterization has been performed to examine thermal stability of P- and N-based alloys and their interaction with interconnect diffusion barrier(s) and solder. At present, we have completed the 7-days aging experiments for 36 tiles, from ambient to 250°C. The thermal behavior of P- and N-based alloys and their thermal interaction with both Ni and Co diffusion barriers and Au–Sn solder were examined.

The preliminary results show the microstructure, texture, alloy composition, and hardness of P–(Bi,Sb)<sub>2</sub>Te<sub>3</sub> and N–Bi<sub>2</sub>(Te,Se)<sub>3</sub> alloys are thermally stable up to 7 days annealing at 250°C. However, metallurgical reactions between the Ni–phosphor barriers and P-type base alloy were evident at temperatures  $\geq 175^\circ\text{C}$ . At 250°C, the depth (or distance) of the metallurgical reaction and/or Ni diffusion into P–(Bi,Sb)<sub>2</sub>Te<sub>3</sub> is approximately 10–15  $\mu\text{m}$ . This thermal instability makes the Ni–phosphor barrier unsuitable for use at temperatures  $\geq 175^\circ\text{C}$ .

The Co barrier appeared to be thermally stable and compatible with P(Bi,Sb)<sub>2</sub>Te<sub>3</sub> at all annealing temperatures, with the exception of a minor Co diffusion into Au–Sn solder at  $\geq 175^\circ\text{C}$ . The effects of Co diffusion on long-term system reliability and/or the thermal stability of the Co barrier are yet to be determined.

Te evaporation and its subsequent reaction with Au–Sn solder and Ni and Co barriers on the ends of the tiles at temperatures  $\geq 175^\circ\text{C}$  were evident. The Te loss and its effect on the long-term required stoichiometry of P–(Bi, Sb)<sub>2</sub>Te<sub>3</sub> are yet to be understood. The aging experiments of 90 days and 180 days are ongoing and scheduled to be completed in 30 days and 150 days, respectively. Material characterization activities are continuing for the remaining tiles.

## **Acknowledgements**

The author would like to thank Scott Whalen, the principal investigator of the project for his technical and funding support. In addition, the programmatic guidance and support from Tim Shepodd, Davina Kwon, Bill Even, Paul Spence, and Rion Causey are greatly appreciated.

# Contents

<b>1. Introduction.....</b>	<b>9</b>
<b>2. Experiment Undertaken.....</b>	<b>11</b>
2.1 Materials.....	11
2.2 Experimental procedures.....	11
2.2.1 Aging experiment.....	11
2.2.2 Material characterization.....	17
2.2.2.1 Sample preparation .....	17
2.2.2.2 Material characterization techniques .....	17
<b>3. Experimental Results .....</b>	<b>18</b>
3.1 Metallurgy and the stability of P- and N-based alloys .....	18
3.1.1 Alloy composition and its thermal stability .....	18
3.1.2 Grain structure and its thermal stability .....	18
3.1.3 Texture and its thermal stability.....	20
3.1.4 Microhardness and its thermal stability .....	21
3.2 Material compatibility and thermal stability of the interconnect materials.....	22
3.2.1 P-(Bi, Sb) <sub>2</sub> Te <sub>3</sub> tile with Ni diffusion barrier.....	22
3.2.1.1 Ni Barrier on Au-Sn soldered end.....	22
3.2.1.2 Ni-phosphor barrier on P-(Bi, Sb) <sub>2</sub> Te <sub>3</sub> tile at the non-soldered end.....	31
3.2.2 P-(Bi, Sb) <sub>2</sub> Te <sub>3</sub> tile with Co diffusion barrier.....	37
3.2.2.1 Co barrier on Au-Sn soldered end.....	37
3.2.2.2 Co barrier on P-(Bi, Sb) <sub>2</sub> Te <sub>3</sub> tile at the Au-Sn non-soldered end.....	41
<b>4. Summary and Discussions .....</b>	<b>45</b>
<b>5. Conclusions.....</b>	<b>48</b>
<b>6. Future Work .....</b>	<b>49</b>

# Figures

<b>Figure 1.</b>	Typical configuration of the commercial TE modules (upper). Material science issues encountered are illustrated in the lower quadrants. ....	10
<b>Figure 2.</b>	(a) Tile geometry, (b) schematic of the tile construction. ....	12
<b>Figure 3.</b>	Sample loading device; the vacuum canister is on the left, and the sample stack assembly is on the right.....	15
<b>Figure 4.</b>	A schematic illustrates the sample designation scheme.....	16
<b>Figure 5.</b>	Preparation of the sample surface. ....	17
<b>Figure 6.</b>	SEM/BEI images show the typical grain structure of P-(Bi,Sb) <sub>2</sub> Te <sub>3</sub> and N-Bi <sub>2</sub> (Te,Se) <sub>3</sub> at various aging temperatures. The darkened speckles seen are pores. ....	19
<b>Figure 7.</b>	EBSF showing the crystallographic orientation of grains relative to geometrical directions of the P-(Bi,Sb) <sub>2</sub> Te <sub>3</sub> tile. ....	20
<b>Figure 8.</b>	EBSF showing the crystallographic orientation of grains relative to the geometrical directions of the N-Bi <sub>2</sub> (Te,Se) <sub>3</sub> tile.....	21
<b>Figure 9.</b>	(a) Digital image shows discoloration of the Au-Sn solder surface at ≥175°C; (b) the metallographic polished cross section. ....	23
<b>Figure 10.</b>	SEM image showing Oswald ripening of the lamellar eutectic Au-Sn solder. The left insert arrow shows the thin reaction layer at the Ni/Ni-phosphor interface at 175°C.....	24
<b>Figure 11.</b>	EDS spectra show the chemical elements present in each reaction layer. ....	25
<b>Figure 12.</b>	SEM images show the microstructure of the reaction zones: (a) SEI image of multiple layered reaction zones, (b) BEI image of the bright second phase reaction front toward P-(Bi, Sb) <sub>2</sub> Te <sub>3</sub> alloy. The upper insert shows the thin darkened reaction layers on both sides of the unreacted Ni-phosphor barrier. ....	26
<b>Figure 13.</b>	X-ray maps show the chemical distribution of each characteristic element at Ni-phosphor/Au-Sn/P-(Bi,Sb) <sub>2</sub> Te <sub>3</sub> interfaces. ....	29
<b>Figure 14.</b>	WDS profiles show diffusion distance at various annealing temperatures. At 250°C, the diffusion distance is ~15 μm. ....	30
<b>Figure 15.</b>	The complementary SEI/BEI image pair shows layered reaction zones on both the soldered and non-soldered ends. ....	32
<b>Figure 16.</b>	SEI/BEI images paired with the upper insert show the multiple reaction layers. The darkened layer in the insert is the P-enriched reaction phase.....	33
<b>Figure 17.</b>	EDS shows the chemical characteristics of each reaction layer.....	34
<b>Figure 18.</b>	X-ray maps show the chemical enrichment for each of the reaction features observed in the tile with an Ni-phosphor barrier. The corresponding SEI/BEI image pair is shown at the lower bottom.....	35
<b>Figure 19.</b>	SEI images together with WDS composition profiles show the ~12-μm deep reaction zones in the tiles subjected to 250°C annealing. ....	36

<b>Figure 20.</b>	The SEI/BEI image pairs show Oswald Ripening of the lamellar Au–Sn eutectic structure. Note: the metallurgical reaction is absent in the P–(Bi, Sb) <sub>2</sub> Te <sub>3</sub> tile with Co barrier at the Au–Sn solder end. ....	38
<b>Figure 21.</b>	EDS spectra of each reaction feature. ....	39
<b>Figure 22.</b>	X-ray maps show the chemical enrichment for each reaction feature in the tile with a Co barrier. The corresponding SEI/BEI image pair is shown at the lower bottom. ....	40
<b>Figure 23.</b>	SEI images at the Co/P(Bi,Sb) <sub>2</sub> Te <sub>3</sub> interface and the WDS composition profiles across the Co/P–(Bi,Sb) <sub>2</sub> Te <sub>3</sub> interfaces; (a–b) As-received; (c–d) annealed at 250°C.....	41
<b>Figure 24.</b>	SEI and BEI images show absence of the metallurgical reaction at the Co/P–(Bi,Sb) <sub>2</sub> Te <sub>3</sub> interface. ....	42
<b>Figure 25.</b>	X-ray maps show absence of the metallurgical reaction and the coexistence of Te and Au on the tile surface for the tile with Co barrier at the non-soldered end. ....	43
<b>Figure 26.</b>	WDS composition profiles show uniform alloy composition of all the characteristic elements across the P-base alloy tight up to the Co/P(Bi,Sb) <sub>2</sub> Te <sub>3</sub> interface. ....	44
<b>Figure 27.</b>	SEI/BEI images and schematics show the severe metallurgical reaction of the Ni–phosphor barrier with the P-based alloy at both the soldered and non-soldered ends. ....	45
<b>Figure 28.</b>	WDS composition profiles show the metallurgical reaction of the P-based alloy with Ni –phosphor, but not the Co barrier. ....	46
<b>Figure 29.</b>	Te and Au x-ray maps show the coexistence of Te and Au on the tile at the non-soldered end. ....	47

## Tables

<b>Table 1.</b>	Samples being characterized. ....	13
<b>Table 2.</b>	Total sample pool: sample matrix for aging experiments.....	14
<b>Table 3.</b>	Alloy composition (at %) at various aging temperatures by WDS.....	18
<b>Table 4.</b>	Vickers test results of aging study for C5. ....	22
<b>Table 5.</b>	Semi-quantitative chemical composition estimated by EDS: wt% of features in P-tile with an electroless Ni–barrier at the solder end. ....	28
<b>Table 6.</b>	Semi-quantitative chemical composition (wt%) for each reaction layer by EDS.....	31
<b>Table 7.</b>	Semi-quantitative chemical composition (wt%) of each reaction feature by EDS.....	39
<b>Table 8.</b>	Samples to be characterized in FY09–FY10.....	50

This page intentionally left blank.

# 1. Introduction

In FY08, the Department 8651 conducted an extensive scientific investigation of several commercial thermoelectric (TE) modules to determine whether they meet Sandia National Laboratories' technical requirements (Figure 1 – upper). The study had confirmed the material suite used in the construction of TE modules for SNL application. In general, metallurgical characteristics of P- and N-based alloys were relatively stable up to 200°C; yet the potential failure modes of the TE modules at  $\geq 160^\circ\text{C}$  for 2 hours were discovered (Ref. 1). In fact, several TE modules had lost their integrity at  $\geq 160^\circ\text{C}$ , a temperature lower than vendors suggested. This loss of integrity was attributed to the metallurgical reaction between the Sn–Sb solder and the  $\text{Bi}_2\text{Te}_3$ -based TE alloys (Figure 1 – lower left). A similar material compatibility issue between diffusion barrier, solder, and P- and N-based alloys was found and studied by others (Refs. 2, 3). (Another finding of interest is the unusual texture of the P and N legs (Figure 1 – lower right), although exploring this issue is beyond the scope of this report).

The above thermally induced TE module failure had raised SNL concerns for long-term reliability of the materials and system design of commercial TE modules for elevated temperature uses. This concern led to material compatibility and thermal aging studies to gain better scientific insight into the material–device interaction within a TE module. The ultimate goal is to determine the specifications for material design and system construction of TE modules based on a sound science. An extensive array of parametric thermal aging experiments were designed for P– $(\text{Bi,Sb})_2\text{Te}_3$  and N– $\text{Bi}_2(\text{Te,Se})_3$  base alloys with Pd, Co and Ni diffusion barriers and Au–Sn solder. Comprehensive material characterization to examine the metallurgy of  $\text{Bi}_2\text{Te}_3$ -based TE alloys and the metallurgical stability of TE materials upon thermal aging is one of the major milestones for the project. The experimental progress and preliminary results from the FY09 activities are documented in this report.

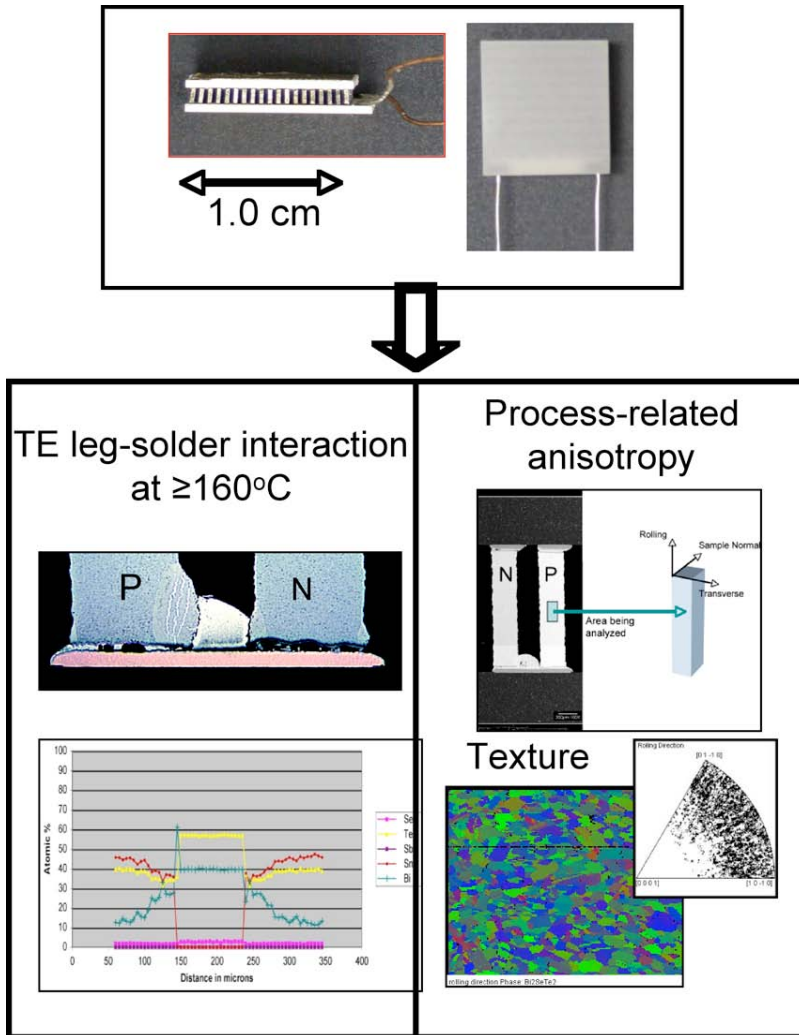


**Figure 1.** Typical configuration of the commercial TE modules (upper). Material science issues encountered are illustrated in the lower quadrants.

## 2. Experiment Undertaken

### 2.1 Materials

One-hundred eight TE tiles were prepared by a commercial vendor specifically for the current aging study. The sample matrix is as follows: a commercial Au (80 at%)–Sn (20 at%) solder and P–(Bi, Sb)<sub>2</sub>Te<sub>3</sub> and N–(Bi)<sub>2</sub>(Te,Se)<sub>3</sub> base alloys. The tiles were electroplated with four different diffusion barriers—Pd, Ni, Co, and Ni—which were electroplated with both electrolytic and electroless processes. The tile geometry, dimensions, and material construction are the same for all tiles, as illustrated in Figure 2 (a–b). The tile dimensions are 5 mm wide x 4 mm height x 2 mm thick. The aging experiments include three aging durations: 7 days, 90 days and 180 days, and three aging temperatures: 100°C, 175°C, and 250°C, as shown in Table 1. The highlighted cells in Table 1 indicate those tiles being aged for 7 days. These tiles are examined and discussed in this report.

### 2.2 Experimental procedures

#### 2.2.1 Aging experiment

There are 36 samples for each aging temperature, as listed in Table 2. The sample loading for the aging experiment is described as follows:

Each of the 36 samples was placed in small Al<sub>2</sub>O<sub>3</sub> crucibles, ½ inch in diameter and ½ inch in height. The sample-containing crucibles were placed on four stacked metal shelves, designated as A, B, C and D, which were fastened on four metal stands as illustrated in Figure 3 – right. The entire sample stack assembly was then placed in the vacuum (10<sup>-4</sup> torr) canisters, 6 inches in diameter and 14 inches in height (Figure 3 – left). To accurately track such a high volume of samples, all the locations in each shelf were marked with a specific sample designation, as illustrated by the schematic in Figure 4. The thermal aging was conducted in a standard furnace chamber with vacuum canisters.

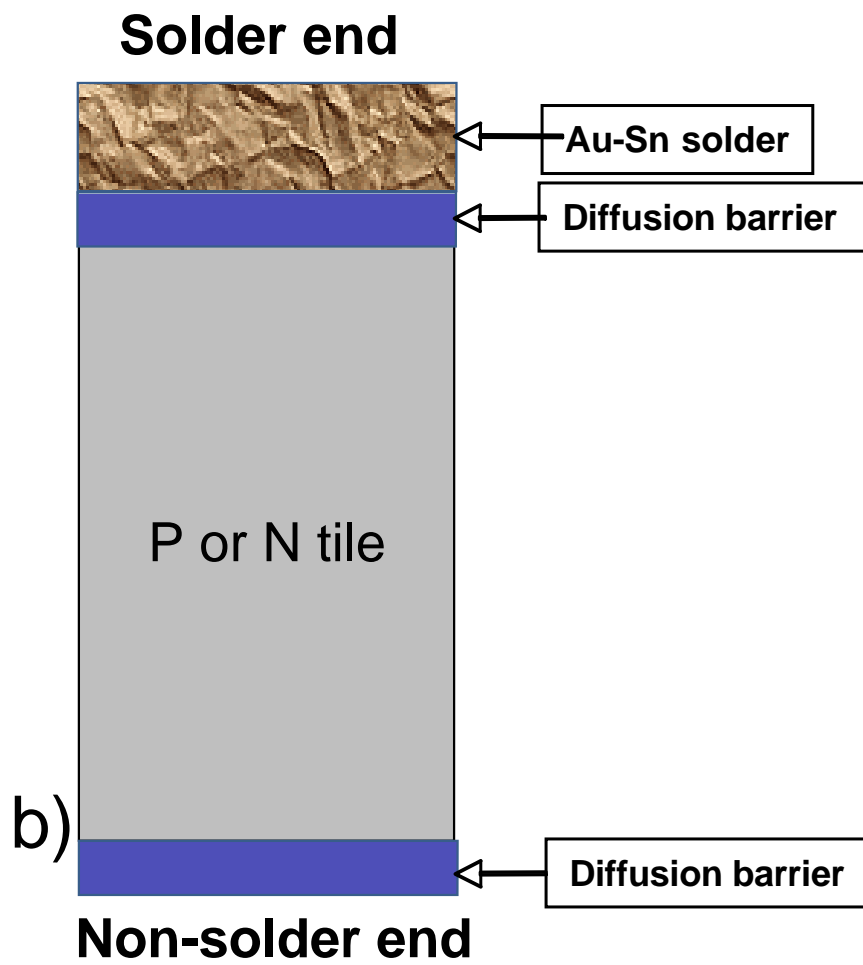
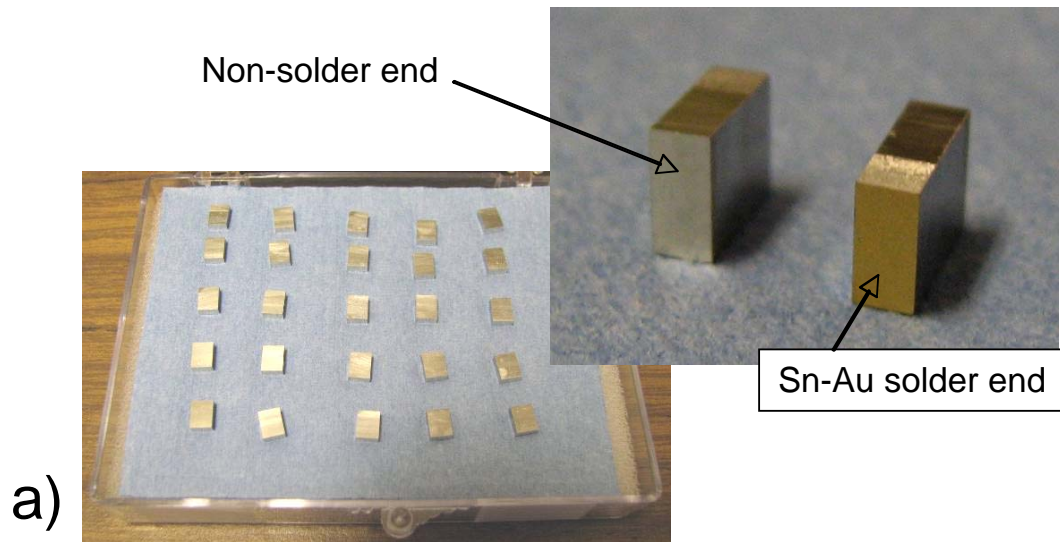


**Figure 2.** (a) Tile geometry, (b) schematic of the tile construction.

**Table 1.** Samples being characterized.

Sample ID	Au-Sn Solder	Temp.(oC)	P-type	N-type
Ni (Electroless)	Solder end	AR	X	X
		100°C	X	X
		175°C	X	X
		250°C	X	X
	Non-solder end	AR	X	X
		100°C	X	X
		175°C	X	X
		250°C	X	X
Co (Electrolytic)	Solder end	AR	X	X
		100°C	X	X
		175°C	X	X
		250°C	X	X
	Non-solder end	AR	X	X
		100°C	X	X
		175°C	X	X
		250°C	X	X
Co (electroless)	Solder end	AR	<b>Aborted due to incorrect chemical composition, i.e. Ni-Co alloy</b>	
		100°C		
		175°C		
		250°C		
	Non-solder end	AR		
		100°C		
		175°C		
		250°C		
Pd (Electrolytic)	Solder end	<b>N/A</b>		
	Non-solder end	AR	X	X
		100°C	X	X
		175°C	X	X
		250°C	X	X
Pd (Electroless)	Solder end	<b>N/A</b>		
	Non-solder end	AR	X	X
		100°C	X	X
		175°C	X	X
		250°C	X	X

(I can't edit this table, but there are a couple fixes to be made: the degree symbol in the temp. heading should be changed, and the degree signs in the column are very small and they appear to be grey instead of black. Also, the "i.e., Ni-Co" needs the comma after "i.e." –KM)

**Table 2.** Total sample pool: sample matrix for aging experiments.

Location	Canister #1	No. of sample	Temp. (°C)	Time (days)	remark
<b>Stack A</b>					
1.0	P-eless Ni	1.0	100.0	7.0	
2.0	P-eless Ni	1.0	100.0	7.0	
3.0	P-eless Ni	1.0	100.0	7.0	
4.0	P-eless Co	1.0	100.0	7.0	
5.0	P-eless Co	1.0	100.0	7.0	
6.0	P-eless Co	1.0	100.0	7.0	
7.0	P-eless Pd	1.0	100.0	7.0	
8.0	P-eless Pd	1.0	100.0	7.0	
9.0	P-eless Pd	1.0	100.0	7.0	
<b>Stack B</b>					
1.0	P-etic Co	1.0	100.0	7.0	
2.0	P-etic Co	1.0	100.0	7.0	
3.0	P-etic Co	1.0	100.0	7.0	
4.0	P-etic Pd	1.0	100.0	7.0	
5.0	P-etic Pd	1.0	100.0	7.0	
6.0	P-etic Pd	1.0	100.0	7.0	
7.0	Sharma 1	1.0	100.0	7.0	
8.0					
9.0					
<b>Stack C</b>					
1.0	N-eless Ni	1.0	100.0	7.0	
2.0	N-eless Ni	1.0	100.0	7.0	
3.0	N-eless Ni	1.0	100.0	7.0	
4.0	N-eless Co	1.0	100.0	7.0	
5.0	N-eless Co	1.0	100.0	7.0	
7.0	N-eless Co	1.0	100.0	7.0	
6.0	N-eless Pd	1.0	100.0	7.0	
8.0	N-eless Pd	1.0	100.0	7.0	
9.0	N-eless Pd	1.0	100.0	7.0	
<b>Stack D</b>					
1.0	N-etic Co	1.0	100.0	7.0	
2.0	N-etic Co	1.0	100.0	7.0	
3.0	N-etic Co	1.0	100.0	7.0	
4.0	N-etic Pd	1.0	100.0	7.0	
5.0	N-etic Pd	1.0	100.0	7.0	
6.0	N-etic Pd	1.0	100.0	7.0	
7.0	Base P	3.0	100.0	7.0	
8.0	Base N	3.0	100.0	7.0	
9.0					
Vacuum is 10 <sup>-4</sup> Torr					

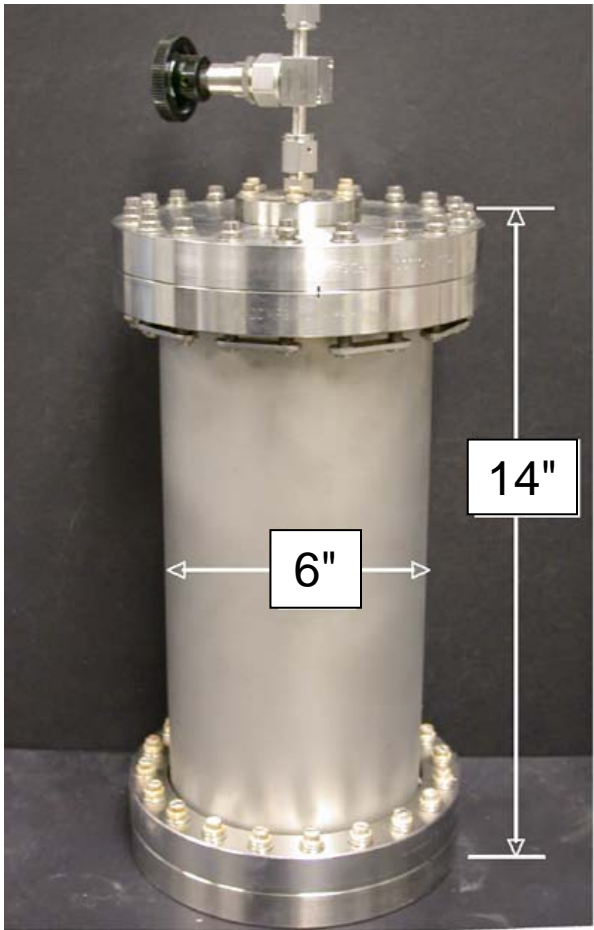


**Figure 3.** Sample loading device; the vacuum canister is on the left, and the sample stack assembly is on the right.

# Reference point

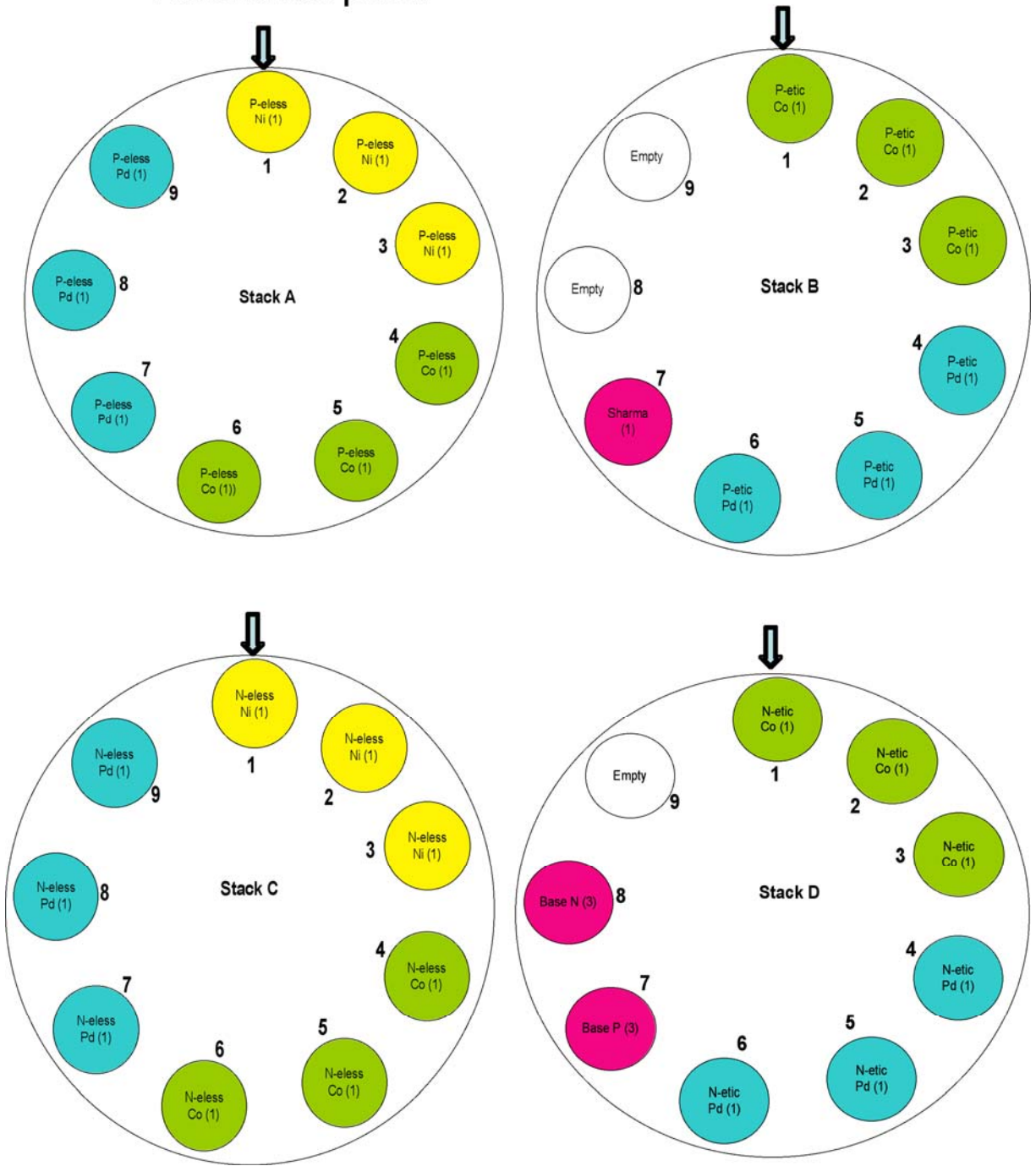


**Figure 4.** A schematic illustrates the sample designation scheme.

## 2.2.2 Material characterization

### 2.2.2.1 Sample preparation

Conventional metallographic mounting, grinding, and polishing were used to prepare the sample surface for the electron optical characterization of the tiles. The metallographic polishing surface was perpendicular to the transverse direction, or through thickness, as illustrated in the following schematic.

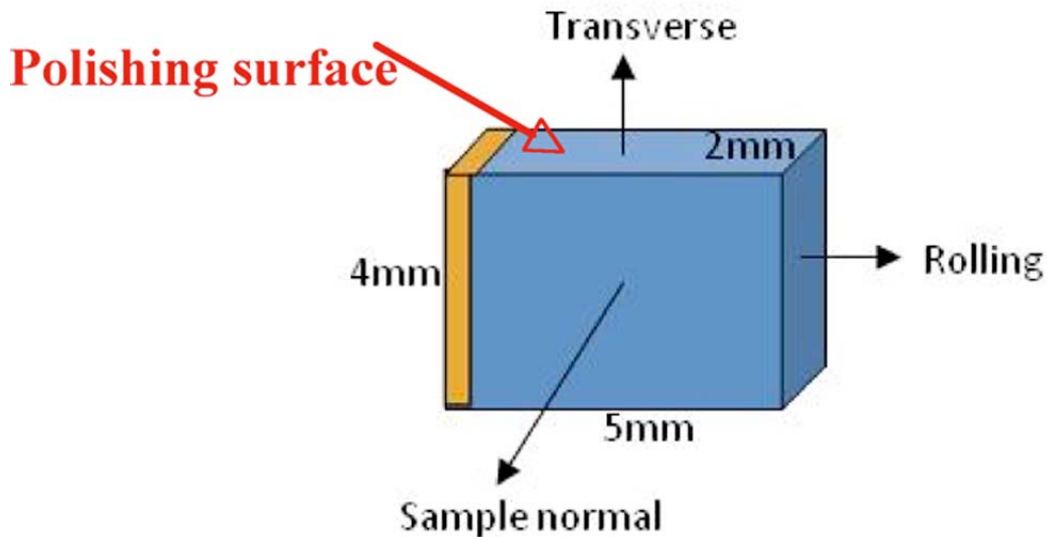


Figure 5. Preparation of the sample surface.

### 2.2.2.2 Material characterization techniques

Material characterization was performed using the following state-of-the-art electron optical and optical metallographic instrumentations:

- **Microstructure:** Scanning electron microscopy (SEM) with secondary electron image (SEI) and/or backscattered electron images (BEI), optical metallographic with polarized light imaging (OP).
- **Alloy composition and elemental diffusion:** Electron probe microanalysis (EPMA) with wavelength dispersive x-ray spectroscopy (WDS) or SEM with energy dispersive x-ray spectroscopy (EDS).
- **Texture of base alloys:** SEM with electron backscattered diffraction pattern (EBSP) utilizing color-coded orientation mapping and an inverse pole figure. The three sample axes were arbitrarily defined by the equipment manufacturer as sample normal (along the sample width, parallel to electron beam direction), transverse (along the tile height) and rolling (along the tile length).
- **Microhardness of base alloys:** Vicker's diamond-indentation with a 10-gram load.

### 3. Experimental Results

#### 3.1 Metallurgy and the stability of P- and N-based alloys

Alloy composition, grain structure, texture, and hardness, as well as the thermal stability of P- and N-based alloys were examined. The experimental results are described below.

##### 3.1.1 Alloy composition and its thermal stability

Alloy composition of P- and N-based alloys were measured by WDS at the center of the tiles. The measured elemental composition matches closely with compound formulation of  $(\text{Bi}_{0.2}\text{Sb}_{0.8})_2\text{Te}_3$  and  $\text{Bi}_2(\text{Te}_{0.85}\text{Se}_{0.15})_3$  for P-type and N-type base alloys, respectively (Table 3). There is minimal change in the composition of either P- and N-based alloys with aging temperatures. For the sake of brevity, the P-type and N-type base alloy are referred as P- $(\text{Bi,Sb})_2\text{Te}_3$  and  $\text{Bi}_2(\text{Te, Se})_3$  in the following discussions.

**Table 3.** Alloy composition (at %) at various aging temperatures by WDS.

Average Atomic % or Center of P Type				
	Te	Sb	Bi	Total
AR	59.72	32.42	7.86	100.00
100°C	59.88	31.13	8.99	100.00
175°C	59.88	31.89	8.23	100.00
250°C	59.93	31.30	8.76	100.00
Average Atomic % or Center of N Type				
	Te	Sb	Bi	Total
AR	52.90	6.15	40.98	100.00
100°C	52.53	6.46	41.01	100.00
175°C	52.54	6.45	41.01	100.00
250°C	52.45	6.50	41.05	100.00

##### 3.1.2 Grain structure and its thermal stability

Optical images show that the grain size and morphology between the as-received P- $(\text{Bi,Sb})_2\text{Te}_3$  and N- $\text{Bi}_2(\text{Te,Se})_3$  alloys are comparable: 10–20  $\mu\text{m}$  in size and equiaxed in shape (Figure 6). The grains in the N-type alloy may be slightly elongated and oriented (Figure 6 – upper left). There are 1–2  $\mu\text{m}$  sized pores, which appear as darkened speckles in the OP images, in both P- and N-based alloys (Figure 6 – light arrow). The pores seem to be much denser and larger in the N-type alloy. Upon thermal aging, no visible change was observed in grain structure or pore density and distribution, indicating good thermal stability was achieved.

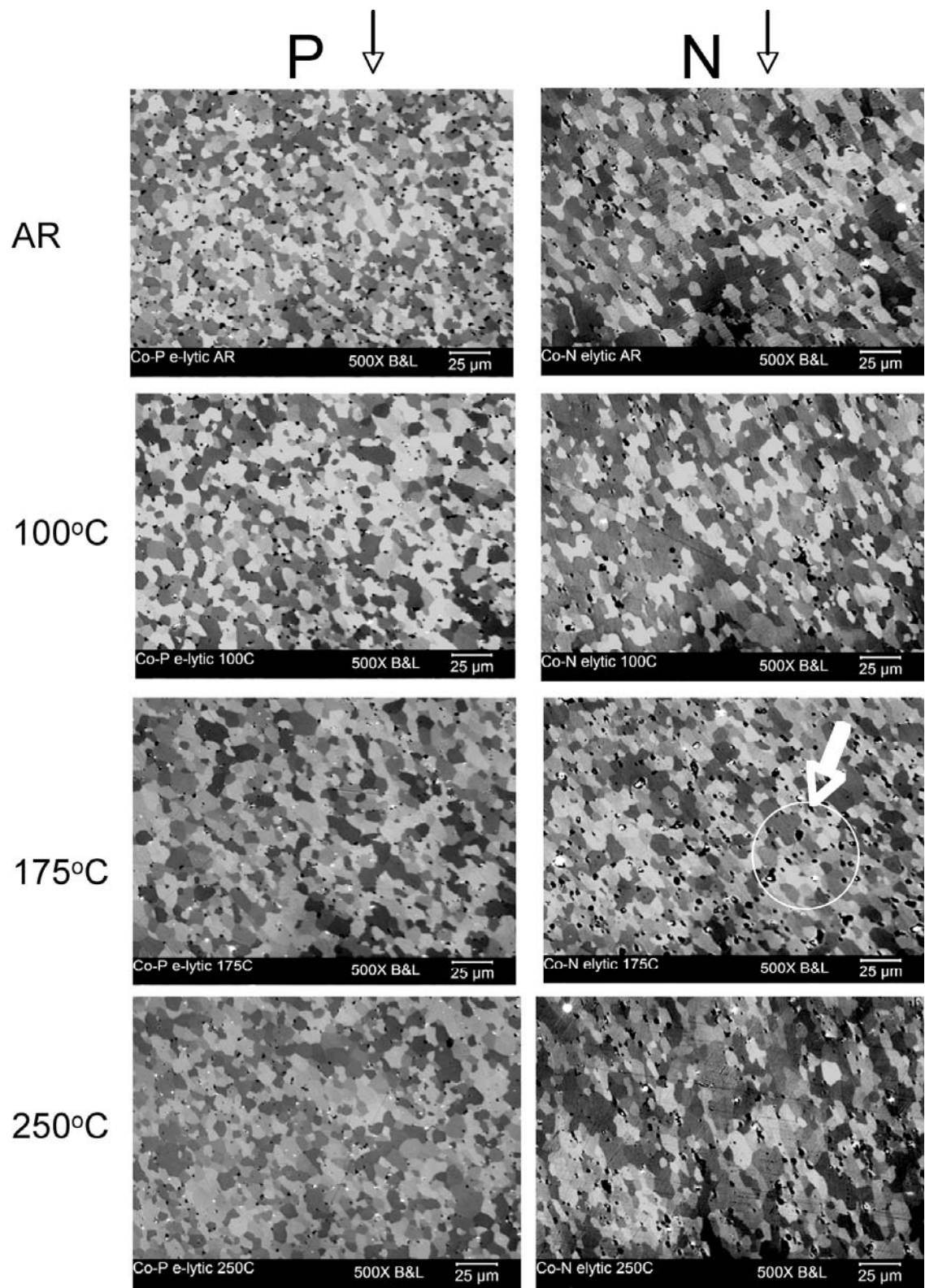


**Figure 6.** SEM/BEI images show the typical grain structure of P-(Bi,Sb)<sub>2</sub>Te<sub>3</sub> and N-Bi<sub>2</sub>(Te,Se)<sub>3</sub> at various aging temperatures. The darkened speckles circled are pores.

### 3.1.3 Texture and its thermal stability

EBSP orientation maps and inverse pole figures show a strong (0,1,1,0) texture in both P- and N-based alloys, along the rolling direction perpendicular to the soldering face. The texture remained the same upon annealing (Figures 7–8). The EBSP maps also have verified the thermally stable grain structure described earlier in Figure 6.

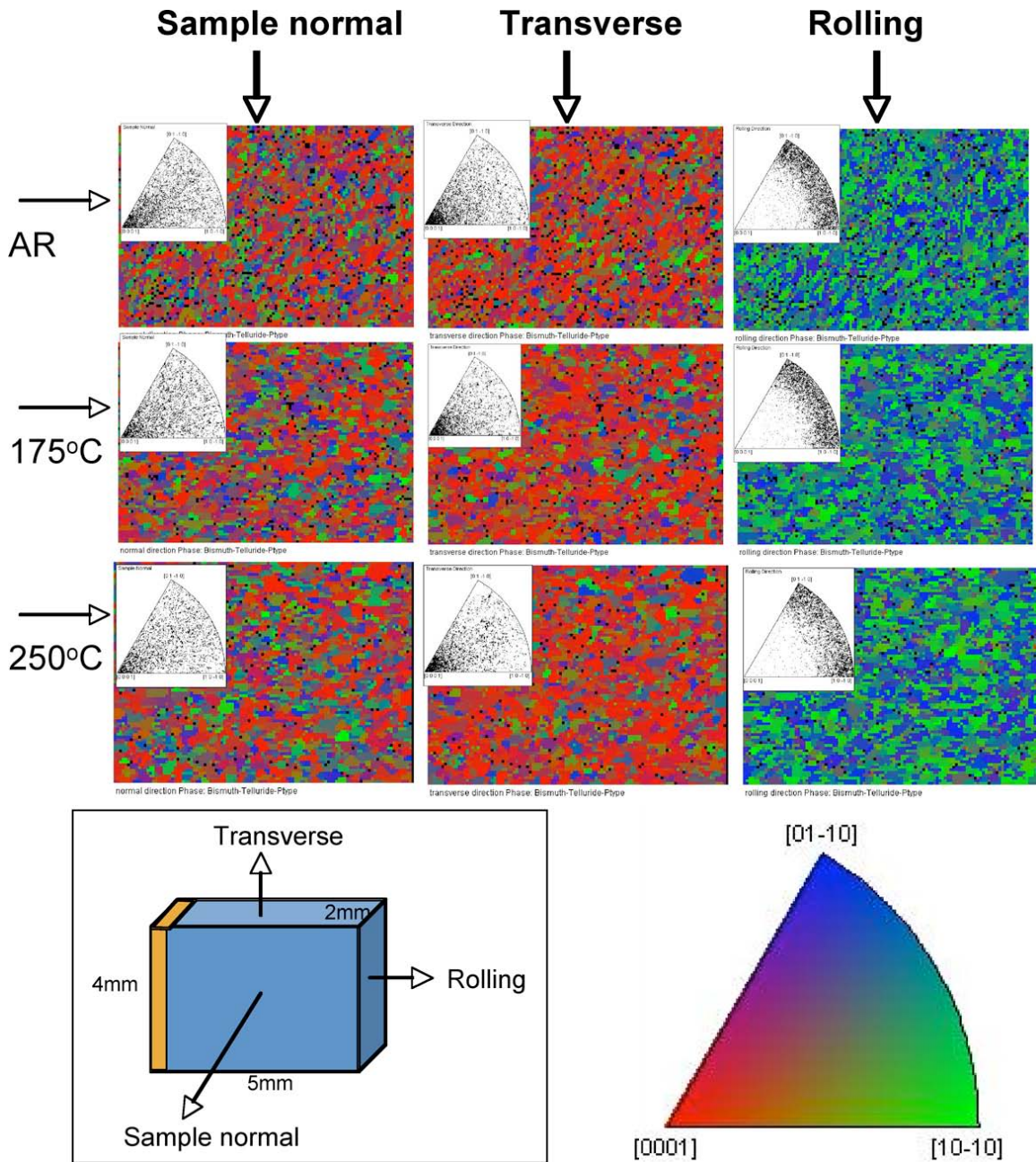


**Figure 7.** EBSP showing the crystallographic orientation of grains relative to geometrical directions of the  $P-(\text{Bi,Sb})_2\text{Te}_3$  tile.

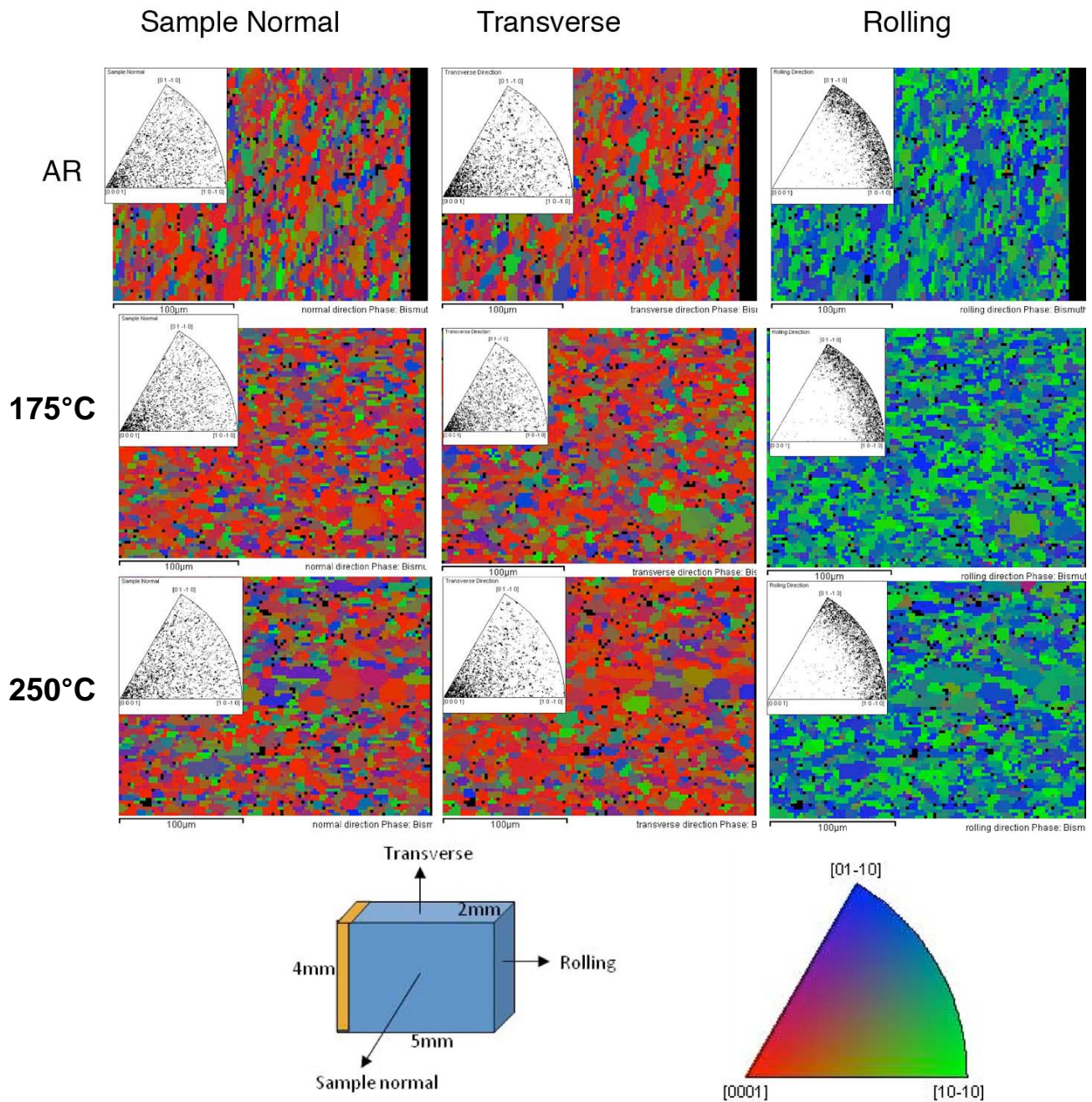


**Figure 8.** EBSD showing the crystallographic orientation of grains relative to the geometrical directions of the  $N\text{-Bi}_2(\text{Te,Se})_3$  tile.

### 3.1.4 Microhardness and its thermal stability

Vickers hardness measured by Vickers diamond indentation show the as-received P- and N-based alloys are very soft, with an average hardness of 50–60 VHN, similar to those measured from wrought Cu (Table 4). The hardness again is comparable throughout all aging

temperatures. The hardness variation seen in Table 4 is within the experimental error attributed to the ill-defined diamond indents of the porous and soft P- and N-based alloys.

**Table 4.** Vickers test results of aging study for C5.

Sample ID	Leg ID	Temp (oC)	Hardness (VHN)
Co (Electrolytic)	P	AR	59.4
		100.0	60.2
		175.0	63.1
		250.0	52.7
	N	AR	48.5
		100.0	65.5
		175.0	57.0
		250.0	53.9

### 3.2 Material compatibility and thermal stability of the interconnect materials

To date, the examination of the thermal behavior has been completed only for Ni and Co diffusion barriers on the P-type tiles, at the non-soldered and the Au–Sn soldered end. The subjects being investigated were potential material interactions, i.e., phase transformation, elemental diffusion, and its resulting microstructure. The Ni barriers studied here were electroplated with electroless, and the Co barriers were electroplated with an electrolytic process.

#### 3.2.1 *P*–(Bi, Sb)<sub>2</sub>Te<sub>3</sub> tile with Ni diffusion barrier

##### 3.2.1.1 Ni Barrier on Au–Sn soldered end

###### *Thermal behavior of the Au–Sn solders*

A digital image of the top surface of P alloy with electroless Co barrier shows the Au–Sn solder surface discolored upon thermal annealing at  $\geq 175^\circ\text{C}$  (Figure 9 – arrow). The solder discoloration indicates a simple solder melting and/or metallurgical reaction with or without other element(s) underneath. The optical images of the polished cross sections show the tile construction consisting Au–Sn solder with diffusion barrier on one end and diffusion barrier only on the other end (Figure 9b).

SEI/BEI images show that the Au–Sn solder thickness varied from 20–50  $\mu\text{m}$ , and contains a lamellar eutectic structure consisting of Au-rich and Sn-rich phases (Figure 10 (a) and Figure 11 Points 9 and 10). The eutectic lamella structure in the as-received tile is finely spaced. The fine eutectic structure had undergone an Oswald Ripening upon thermal annealing. The lamellar spacing was progressively increased from 2–4  $\mu\text{m}$  in the as-received tile to 10–15  $\mu\text{m}$  in the 250°C annealed tile (Figure 10 a-d– arrows).

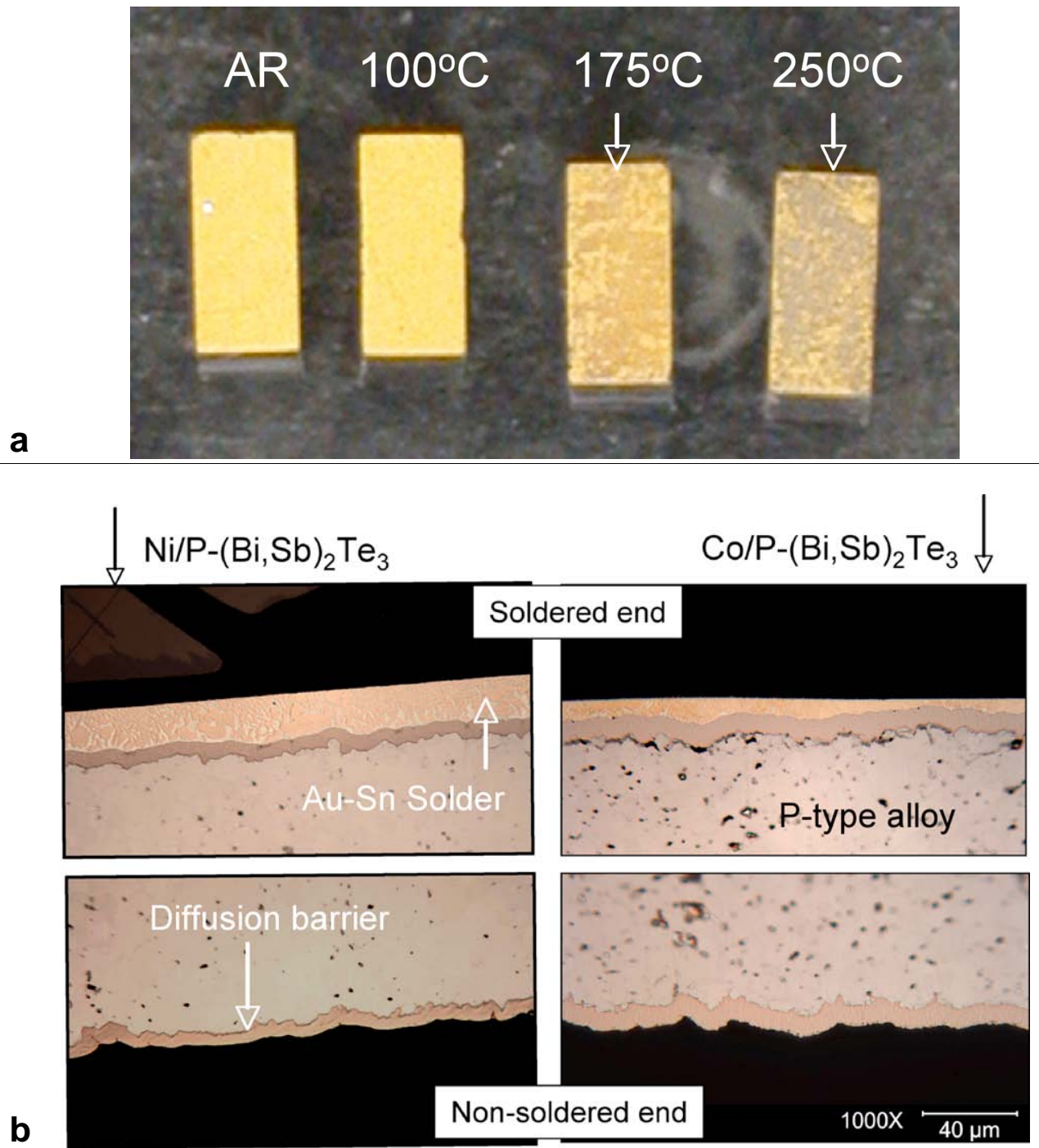


**Figure 9.** (a) Digital image shows discoloration of the Au–Sn solder surface at  $\geq 175^\circ\text{C}$ ; (b) the metallographic polished cross section.

# 175°C-insert

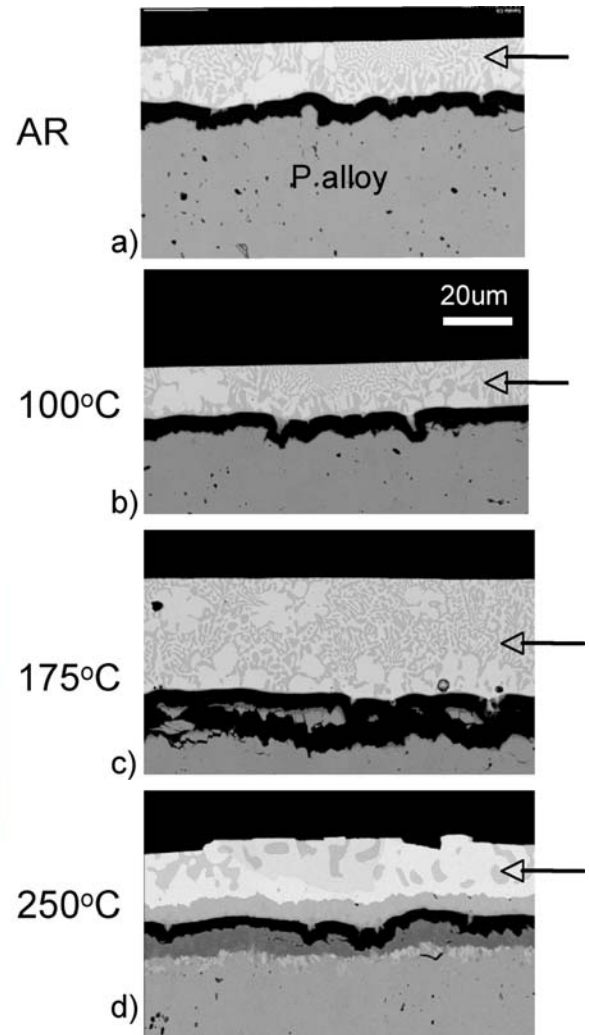
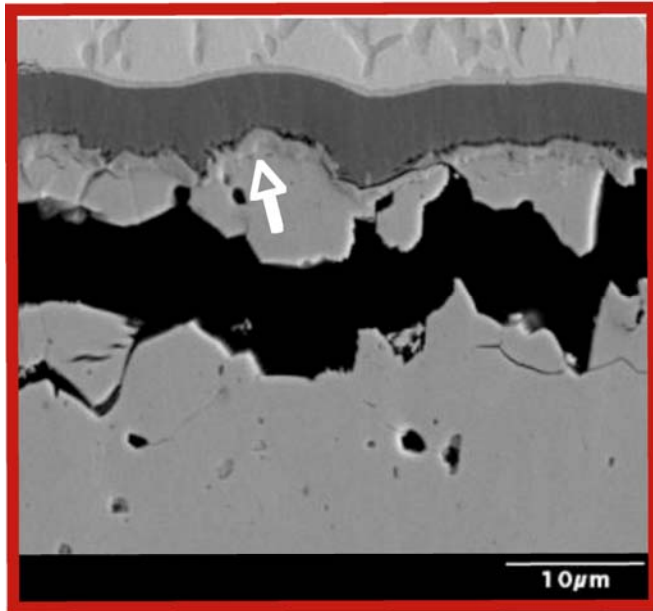


**Figure 10.** SEM image showing Oswald ripening of the lamellar eutectic Au-Sn solder. The left insert arrow shows the thin reaction layer at the Ni/Ni-phosphor interface at 175°C.

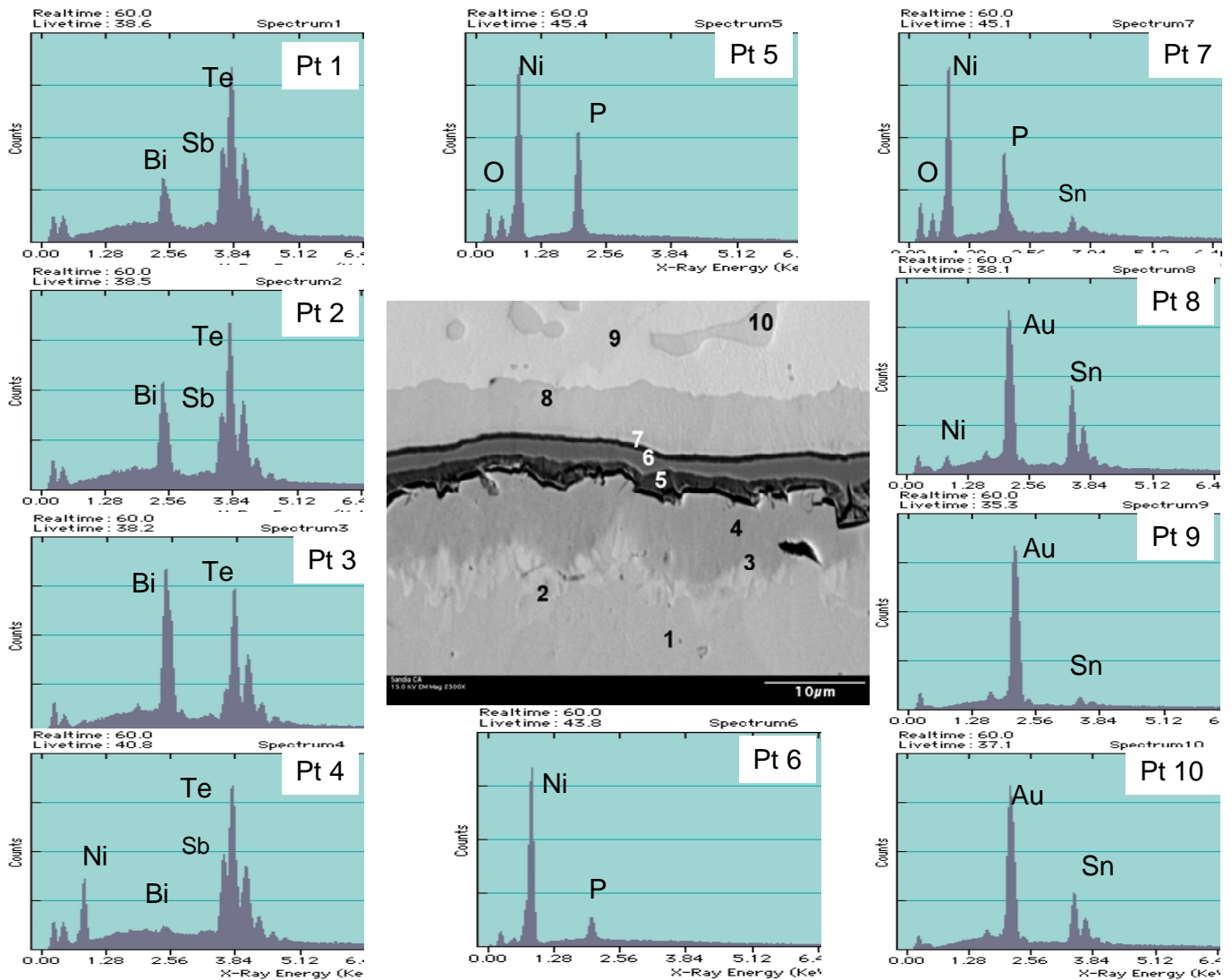


**Figure 11.** EDS spectra show the chemical elements present in each reaction layer.

*Metallurgical reaction among Au–Sn, solder, Ni diffusion barrier and P–(Bi, Sb)<sub>2</sub>Te<sub>3</sub>*

The BEI images in Figure 10 provide a good general view of the overall construction and microstructure of the P-type tile with and Ni diffusion barrier Au–Sn solder. The Ni barrier on the as-received tiles is approximately 5–6  $\mu\text{m}$  beneath 20–50  $\mu\text{m}$  thick (Figure 10(a)). Generally speaking, there is no visible change in microstructure of this triple-layer tile construction at a temperature lower than 175°C for 7 days. The tile that was annealed at 175°C cracked along the solder–barrier interface, and this defect limited the effectiveness of our examination. Fortunately, there is a small area still intact in the 175°C annealed tile where we observed that a minor metallurgical reaction ( $\ll 5 \mu\text{m}$  thick) started, near the Ni/P–(Bi, Sb)<sub>2</sub>Te<sub>3</sub> interface in the P-base alloy side (See Figure 10 left insert – arrow). At 250°C, the complex multiple layered reaction zones were clearly seen across the Au–Sn solder/Ni barrier /P–(Bi, Sb)<sub>2</sub>Te<sub>3</sub> interfaces.

This multilayer microstructure at 250°C is revealed clearly in the complementary SEI and BEI images in Figure 12 (a–b) along with a high-magnification insert. There are two layered reaction zones, ~1.0 μm darkened and ~5μm light grey, at the Au–Sn solder/Ni–phosphor interface toward the solder side. At the Ni–phosphor/P-(Bi, Sb)<sub>2</sub>Te<sub>3</sub> interface, three reaction layers were seen toward P(Bi,Sb)<sub>2</sub>Te<sub>3</sub> side. The thickness for each layer is ~2μm (darkened), ~5μm (grey) and ~2 μm (non-uniform bright), respectively. The bright layer consists of discontinuous second-phase particles with a reaction front toward the P–(Bi, Sb)<sub>2</sub>Te<sub>3</sub> side (Figure 12 (b)—arrow).

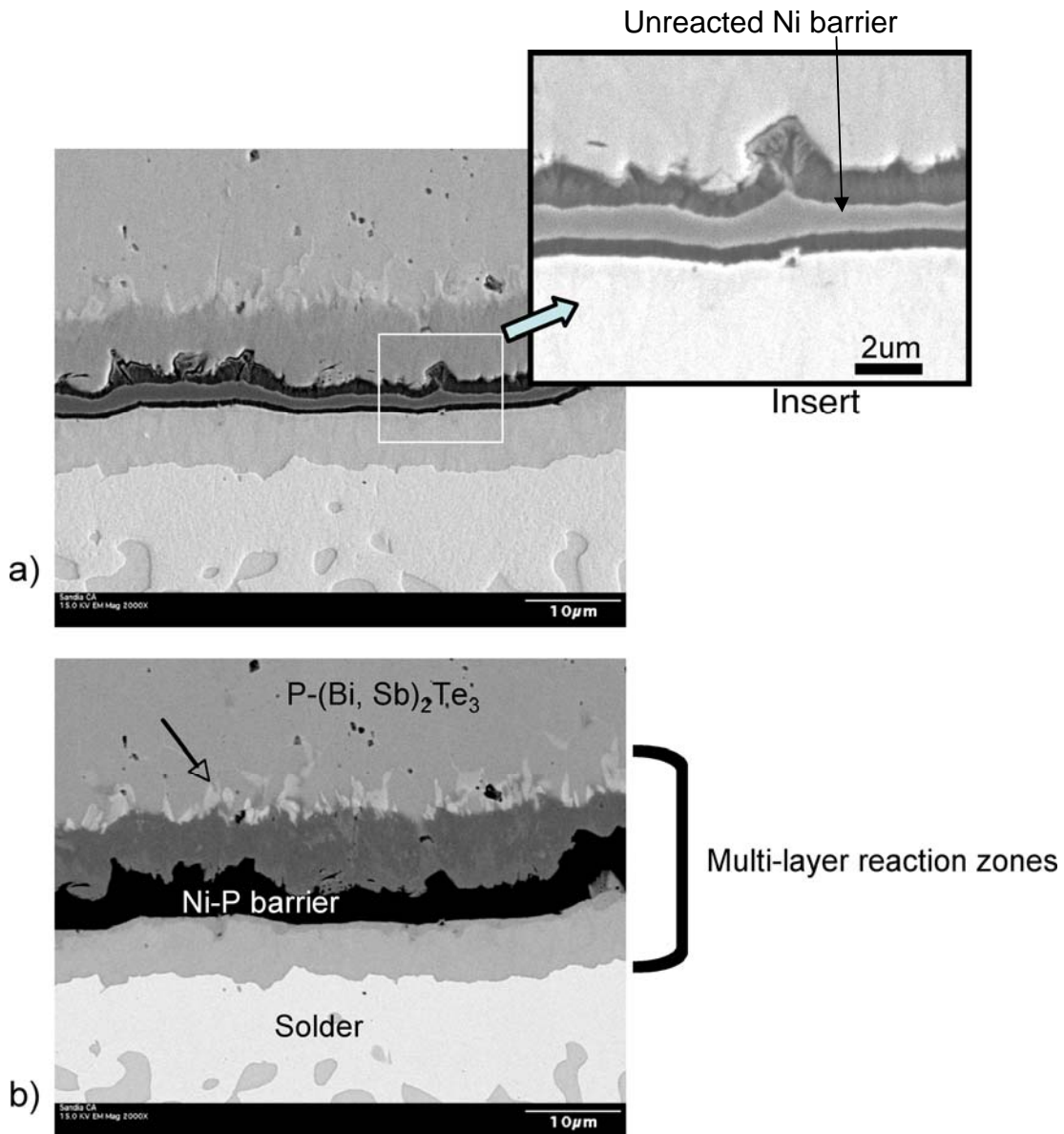


**Figure 12.** SEM images show the microstructure of the reaction zones: (a) SEI image of multiple layered reaction zones, (b) BEI image of the bright second phase reaction front toward P-(Bi, Sb)<sub>2</sub> Te<sub>3</sub> alloy. The upper insert shows the thin darkened reaction layers on both sides of the unreacted Ni-phosphor barrier.

Chemical characteristics of each feature in the reaction zones were measured semi-qualitatively by EDS point analyses. The specific layered reaction zones and their corresponding chemical compositions are displayed qualitatively by EDS spectra in Figure 11, and quantitatively in Table 5. Chemical composition of the P-(Bi,Sb)<sub>2</sub>Te<sub>3</sub> and the two eutectic phases are as expected, as shown in Points 1, 9, and 10 in Figure 11, respectively. The following are the scientific highlights drawn from the above SEM/EDS analyses:

- The actual composition of the Ni barrier is a Ni-phosphor (~5–10 wt%) compound, not pure Ni as given (Table 5 – Point 6).
- The two darkened layers, next to the Ni-barrier, contain high N- and P-phosphor, consistent with the chemical characteristics of Ni-phosphor barrier with a minor addition of oxygen (Figure 11 – Points 5 and 7). The new phosphor-enriched phase appeared to form within the original unreacted N-phosphor barrier space, leading to a 50% reduction in thickness, to 2–3 μm instead of the original 5–6 μm (Figure 12 upper insert – arrow).
- The two light grey layers seen in the Au–Sn solder and P-(Bi,Sb)<sub>2</sub>Te<sub>3</sub> contain Ni in addition to the chemical characteristic of the barrier and P base alloy. (Figure 11 – Points 4 and 8). The Ni diffusion into the P-(Bi, Sb)<sub>2</sub>Te<sub>3</sub> led to the depletion of Te and Sb.
- The discontinuous bright reaction fronts are the new Bi-enriched (>>20 wt%) second-phase particles that precipitated out of the P-(Bi, Sb)<sub>2</sub>Te<sub>3</sub> (Figure 11 – Points 2 and 3).
- The microstructure and chemical change of Au and Sn composition mostly stayed within the solder itself. Elemental Au and Sn were absent in the Ni-phosphor barrier and all other reaction layers on the P-(Bi,Sb)<sub>2</sub>Te<sub>3</sub> side (Figure 11 – Points 1 to 6).

The above findings in chemical characteristics were verified qualitatively by the x-ray maps—for instance, Te and Sb depletion at the interface with Ni-phosphor (Figure 13 – arrows). Note that the high oxygen x-ray intensity on the outer surface (shown in the oxygen x-ray map) is most likely an artifact of the epoxy used for sample mounting.

Length scale of the metallurgical reaction was examined using WDS composition profiles as illustrated in Figure 14. The overall elemental diffusion distance for the tile with the highest aging temperature, 250°C, is 20–25 μm, counting the 2–4 μm unreacted Ni-phosphor barriers. Most significantly, the elemental diffusion distance of Ni into P-(Bi, Sb)<sub>2</sub>Te<sub>3</sub> is ~ 10–15 μm (Figure 14 – bottom box) which is three times deeper than the 2–3 μm defined arbitrarily for the as-received tile (Figure 14 – top box). The WDS profiles also show minimal change in Ni diffusion or metallurgical reaction distance among the as-received tiles and those tiles annealed at ≤ 175°C (Figure 14 – middle two boxes).

**Table 5.** Semi-quantitative chemical composition estimated by EDS:  
wt% of features in P-tile with an electroless Ni-barrier at the solder end.

<b>Location</b>	<b>Bi</b>	<b>Te</b>	<b>Sb</b>	<b>Ni</b>	<b>Co</b>	<b>P</b>	<b>O</b>	<b>Sn</b>	<b>Au</b>
<b>Point 1</b>	13.69	55.45	30.86	-	-	-	-	-	-
<b>Point 2</b>	24.44	52.69	22.86	-	-	-	-	-	-
<b>Point 3</b>	39.57	49.14	11.29	-	-	-	-	-	-
<b>Point 4</b>	1.52	38.16	21.86	38.45	-	-	-	-	-
<b>Point 5</b>	-	-	-	81.32	-	18.21	0.48	-	-
<b>Point 6</b>	-	-	-	95.42	-	4.56	0.02	-	-
<b>Point 7</b>	-	-	-	88.74	-	11.22	0.04	-	-
<b>Point 8</b>	-	-	-	8.59	-	-	-	39.64	51.76
<b>Point 9</b>	-	-	-	-	-	-	-	10.01	89.99
<b>Point 10</b>	-	-	-	-	-	-	-	33.50	66.50

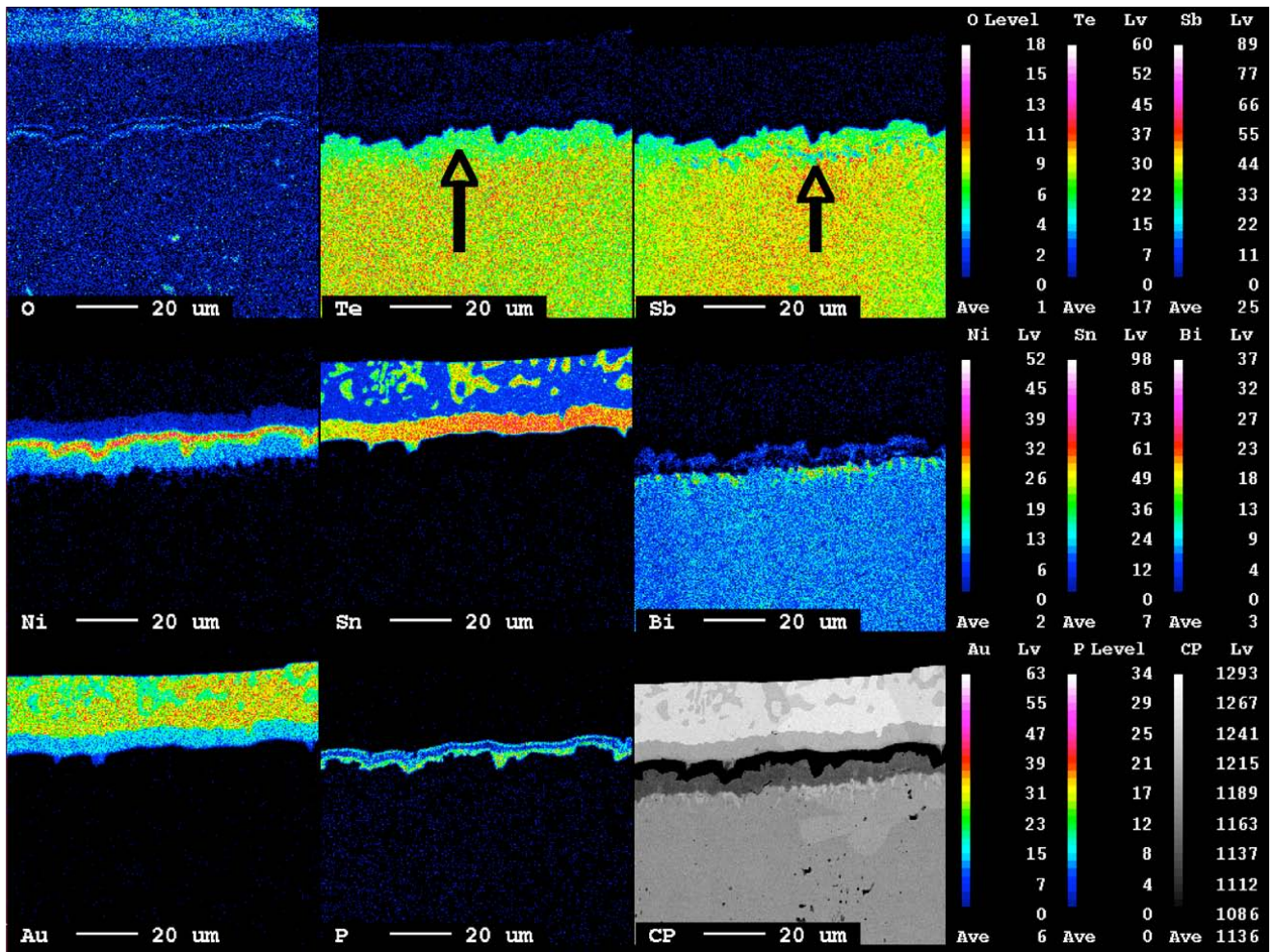


**Figure 13.** X-ray maps show the chemical distribution of each characteristic element at Ni-phosphor/Au-Sn/P-(Bi,Sb)<sub>2</sub>Te<sub>3</sub> interfaces.

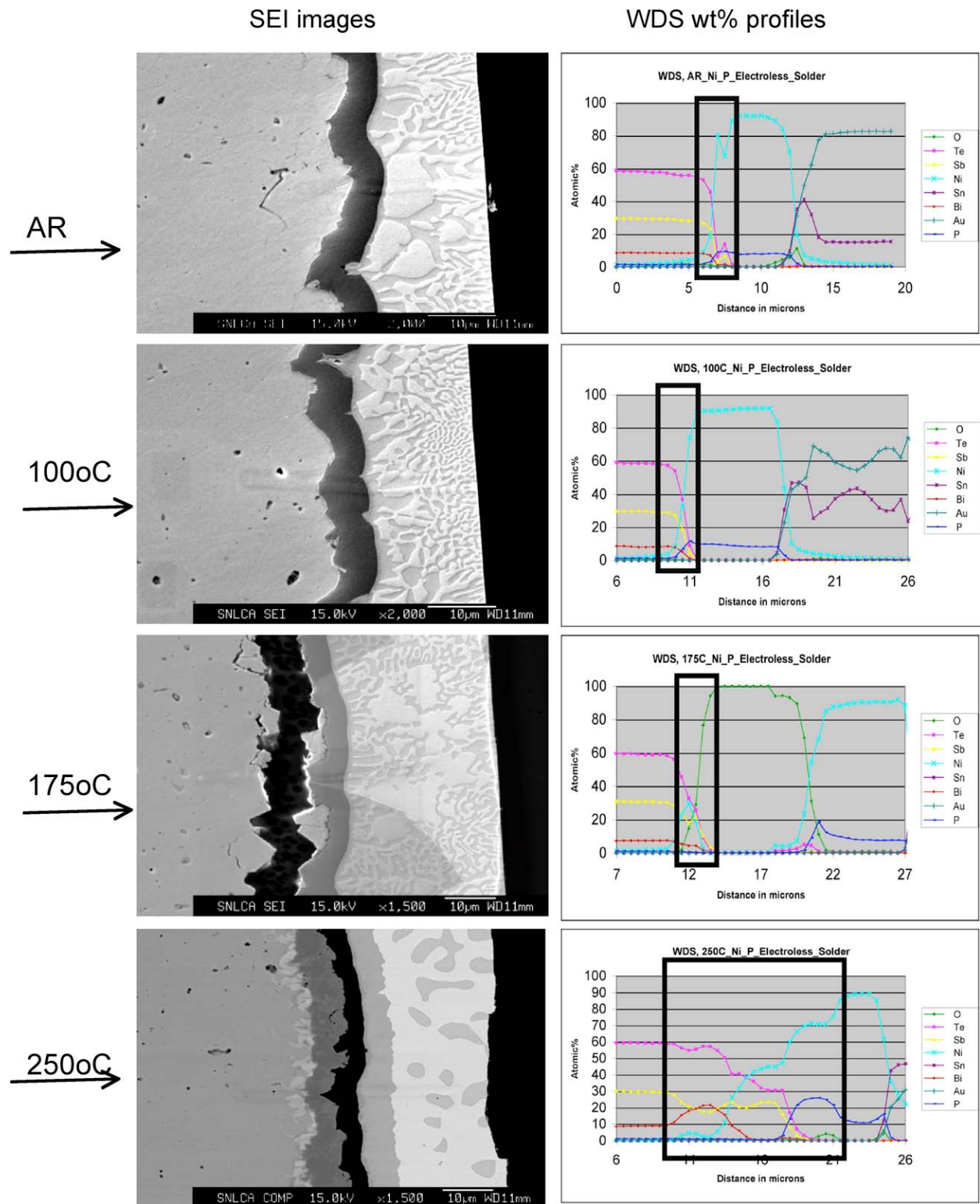


**Figure 14.** WDS profiles show diffusion distance at various annealing temperatures. At 250°C, the diffusion distance is ~15  $\mu\text{m}$ .

### 3.2.1.2 Ni–phosphor barrier on P–(Bi, Sb)<sub>2</sub>Te<sub>3</sub> tile at the non-soldered end

#### *Metallurgical reaction between Ni–phosphor diffusion barrier and P–(Bi, Sb)<sub>2</sub>Te<sub>3</sub>*

Without the Au–Sn solder, the overall microstructure on the non-soldered end was less complex than those seen on the Au–Sn soldered end. Most importantly, the metallurgical reaction at the non-soldered end was quite comparable to those seen on the soldered end for all annealing temperatures. Minimal metallurgical reaction was observed in the tiles annealed at  $\leq 175^\circ\text{C}$ . Similar multiple layered reaction zones were observed at the Ni–phosphor/ P–(Bi, Sb)<sub>2</sub>Te<sub>3</sub> interface for the tile annealed at 250°C. The total depth of the reaction zone is also 10–15  $\mu\text{m}$  deep. The microstructure and the chemical characteristics of each reaction layer were comparable to those seen on the soldered end (Table 6 and Figures 15–18). For instance, the phosphor-enriched phase was present between the Ni–phosphor barrier and P–(Bi,Sb)<sub>2</sub>Te<sub>3</sub> alloy and the Bi-enriched second phase forming at the reaction front toward the P–(Bi,Sb)<sub>2</sub>Te<sub>3</sub>. It is important to note that on the top free surface, there is a Te-rich phase that coexists with the surface Au coating, an integral part of the tile fabrication process (Figure 17 – Point 7 and Figure 18 – arrows). It is unclear how the foreign Te-rich phase gets on the surface. The WDS profiles show slight increases in the reaction depth with annealing temperature (Figure 19 (a–d) – boxes).

**Table 6.** Semi-quantitative chemical composition (wt%) for each reaction layer by EDS.

Ni-P eless nonsoldered									
Location	Bi	Te	Sb	Ni	Co	P	O	Sn	Au
Point 1	13.76	55.13	31.11	-	-	-	-	-	-
Point 2	41.26	55.29	-	3.45	-	-	-	-	-
Point 3	38.57	56.59	-	4.84	-	-	-	-	-
Point 4	2.52	33.29	24.72	39.46	-	-	-	-	-
Point 5	-	-	-	84.39	-	15.57	0.04	-	-
Point 6	-	-	-	95.07	-	4.91	0.03	-	-
Point 7	-	34.84	-	37.66	-	-	-	-	27.50

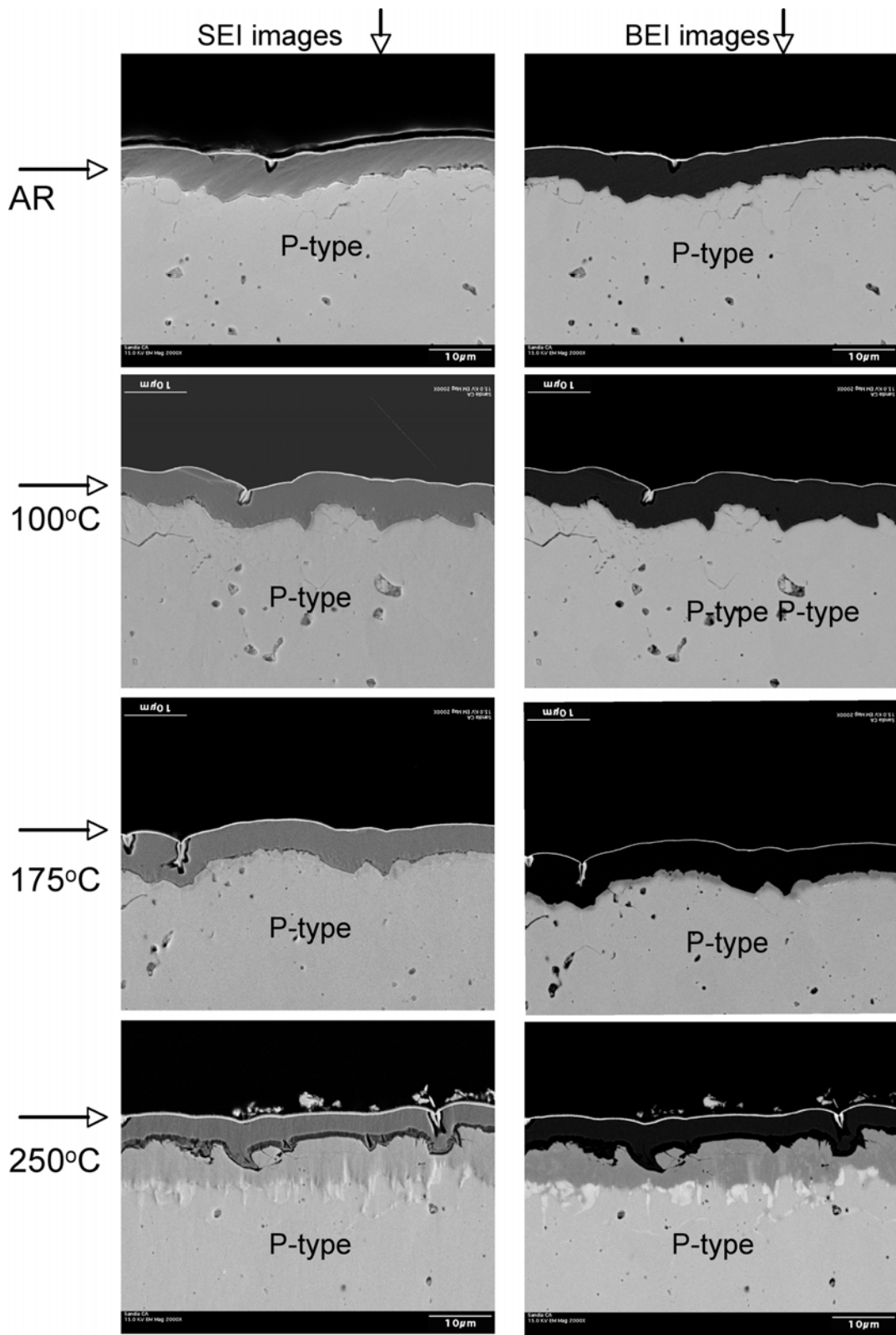


**Figure 15.** The complementary SEI/BEI image pair shows layered reaction zones on both the soldered and non-soldered ends.

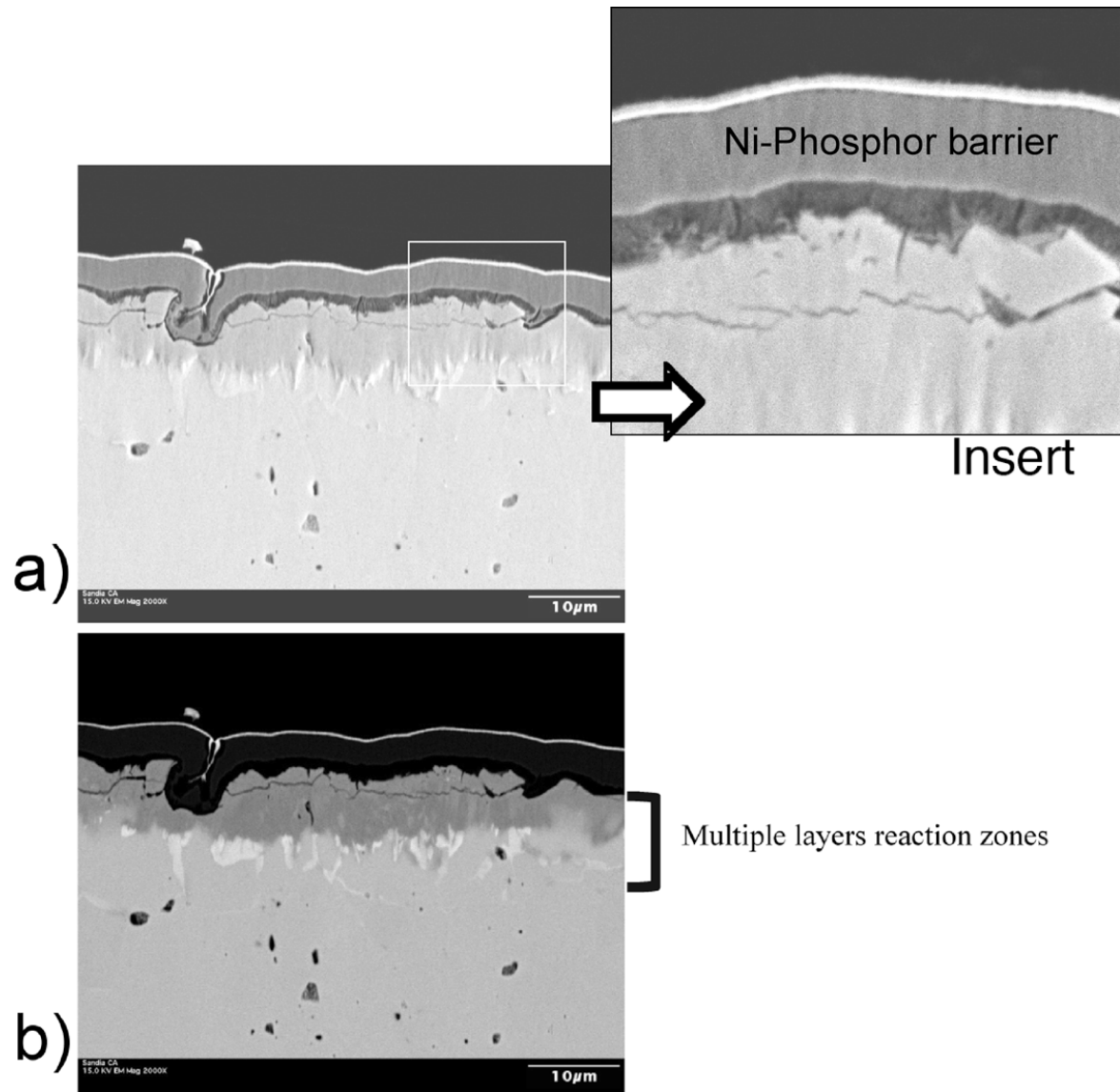


**Figure 16.** SEI/BEI images paired with the upper insert show the multiple reaction layers. The darkened layer in the insert is the P-enriched reaction phase.

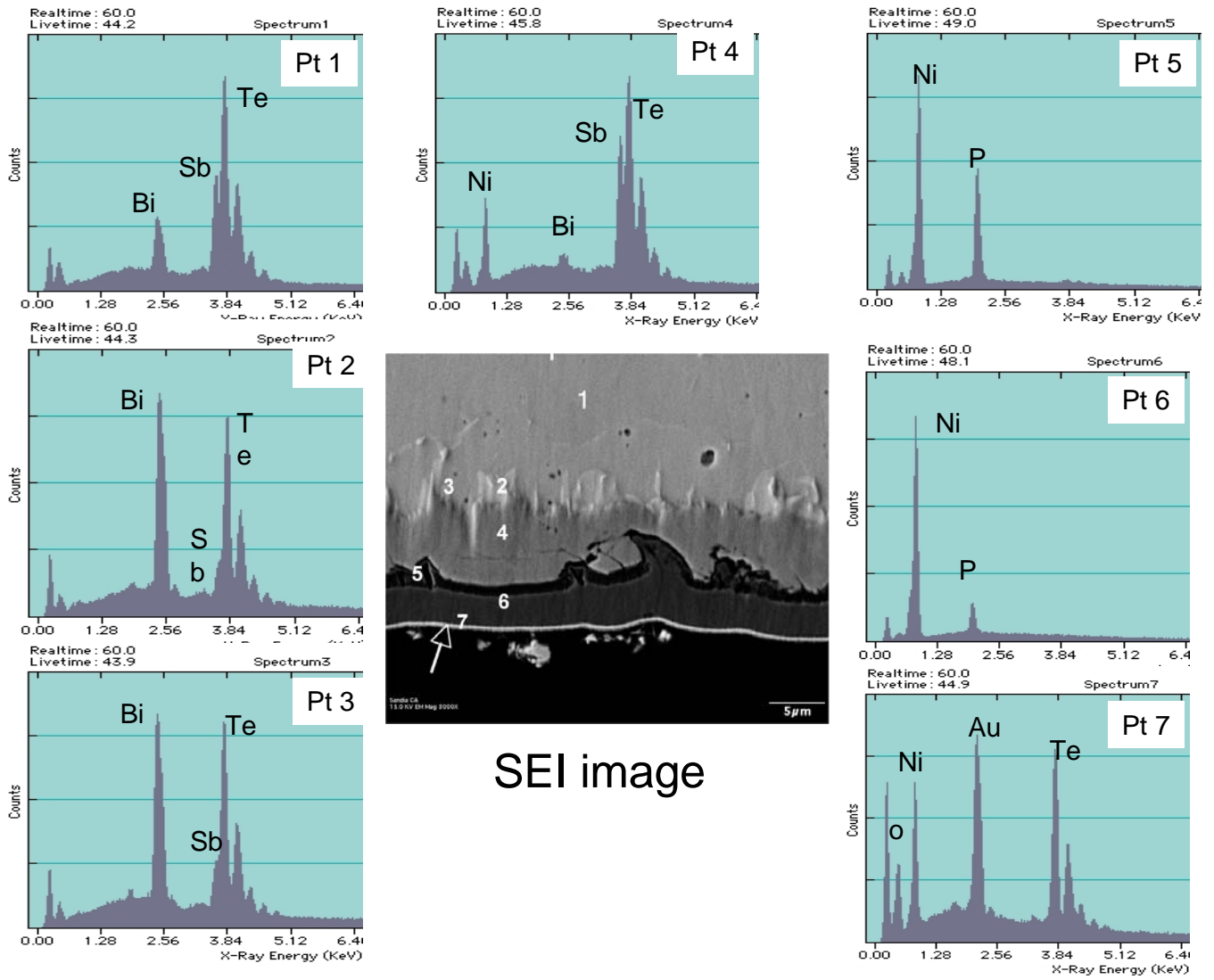


**Figure 17.** EDS shows the chemical characteristics of each reaction layer.

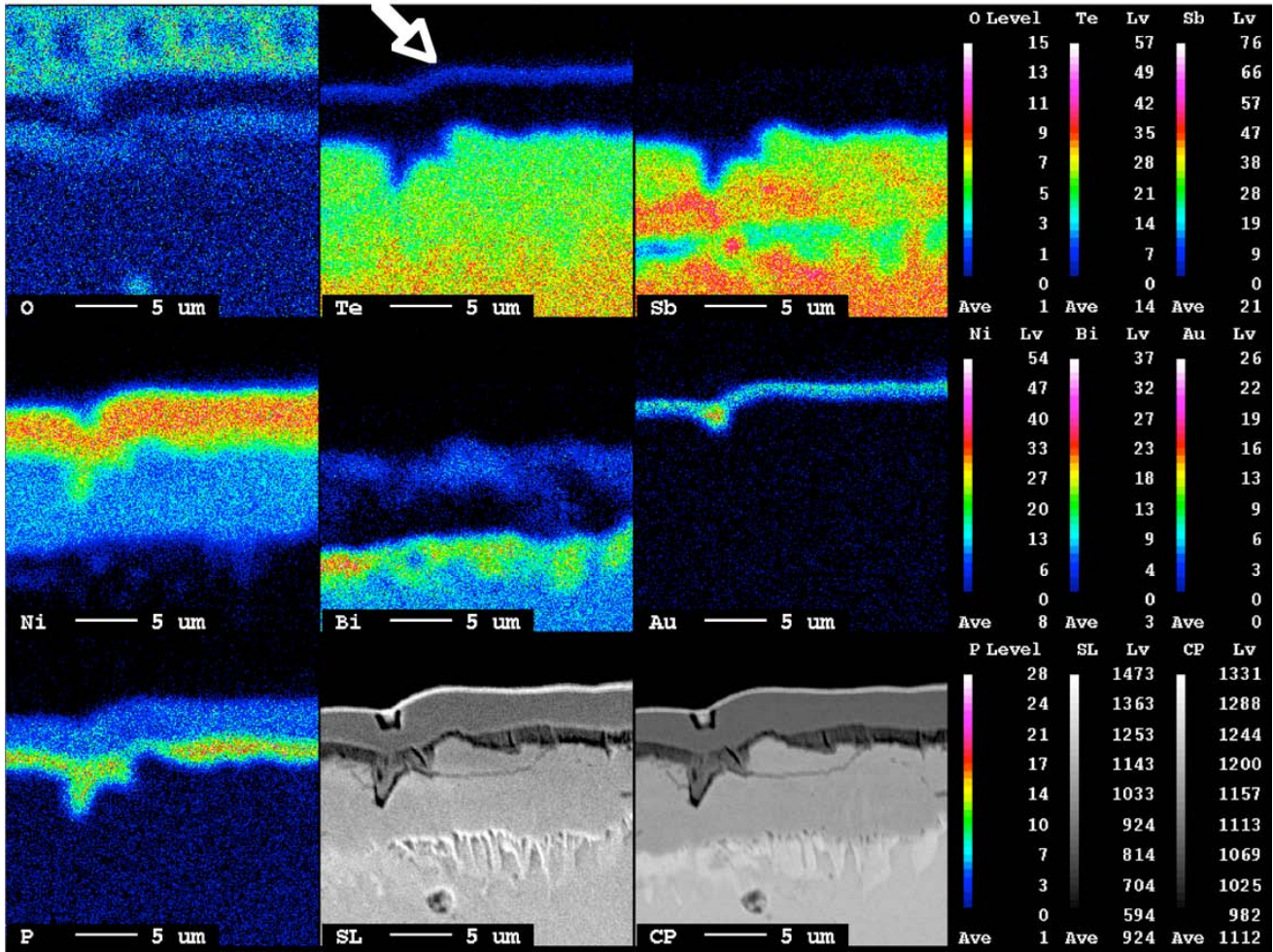


**Figure 18.** X-ray maps show the chemical enrichment for each of the reaction features observed in the tile with an Ni-phosphor barrier. The corresponding SEI/BEI image pair is shown at the lower bottom.

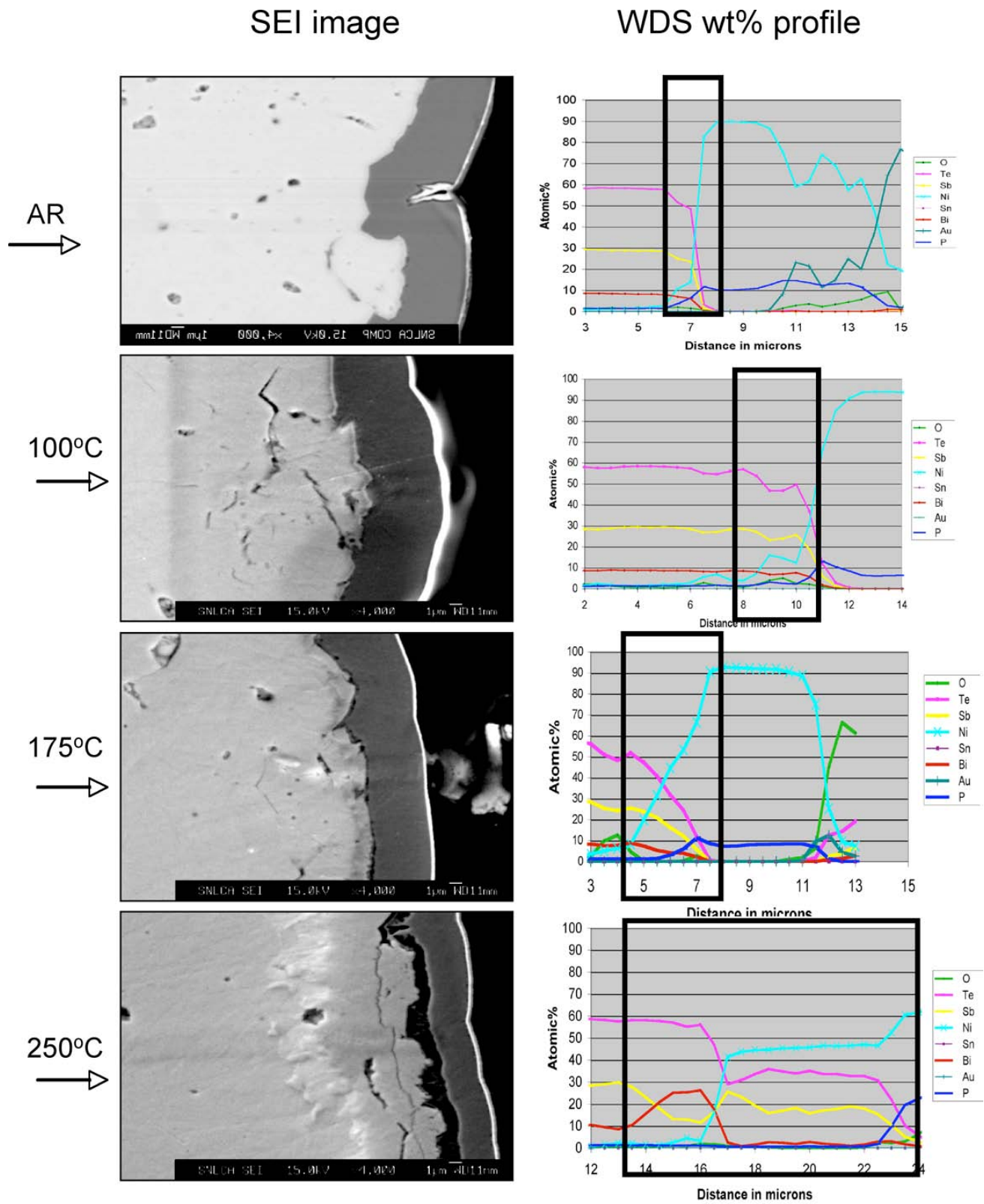


**Figure 19.** SEI images together with WDS composition profiles show the ~12- $\mu\text{m}$  deep reaction zones in the tiles subjected to 250°C annealing.

### **3.2.2 $P-(Bi, Sb)_2Te_3$ tile with Co diffusion barrier**

#### **3.2.2.1 Co barrier on Au–Sn soldered end**

##### Thermal stability of the Au–Sn solders

The thermal behavior of the Au–Sn solder on  $P-Bi_2(Te,Se)_3$  is similar to that described in Section 3.2.1.1; i.e., the Au solder contains two phases, Sn-rich and Au-rich phase, lamellar eutectic structure which undergone Oswald Ripening with much coarser inter-lamellar spacing, 10–15  $\mu\text{m}$  instead of 2–4  $\mu\text{m}$  seen in the as-received solders (Figure 20). SEI/BEI images pair again show the non-uniform thickness of the Au–Sn solder, which could vary from 10 to 40  $\mu\text{m}$  (Figure 20).

##### Metallurgical reactions among Au–Sn solder, Co diffusion barrier and $P-(Bi, Sb)_2Te_3$

Beside the Oswald Ripening of the Au–Sn solder, a thin reaction layer (1  $\mu\text{m}$  thick) was observed at the Co barrier/Au–Sn interface (Figure 21). EDS shows that the layer contains moderate amount of Co, 5–20 wt%, in addition to Au and Sn (Figure 21 – Point 3 and 6). Most significantly, the metallurgical reaction or Co diffusion is absent in  $P-Bi_2(Te,Se)_3$  at all annealing temperatures, as confirmed by EDS, x-ray maps, and WDS composition profiles (Figures 22–24 and Table 7). Note that the x-ray map shows that the Te-enriched phase coexisted with the Au coating on the top surface (Figure 22 – arrows). Additionally, the x-ray map shows that Te is also elevated in the Au–Sn eutectic phase, possibly due to Te diffusion to Au–Sn from the top surface.

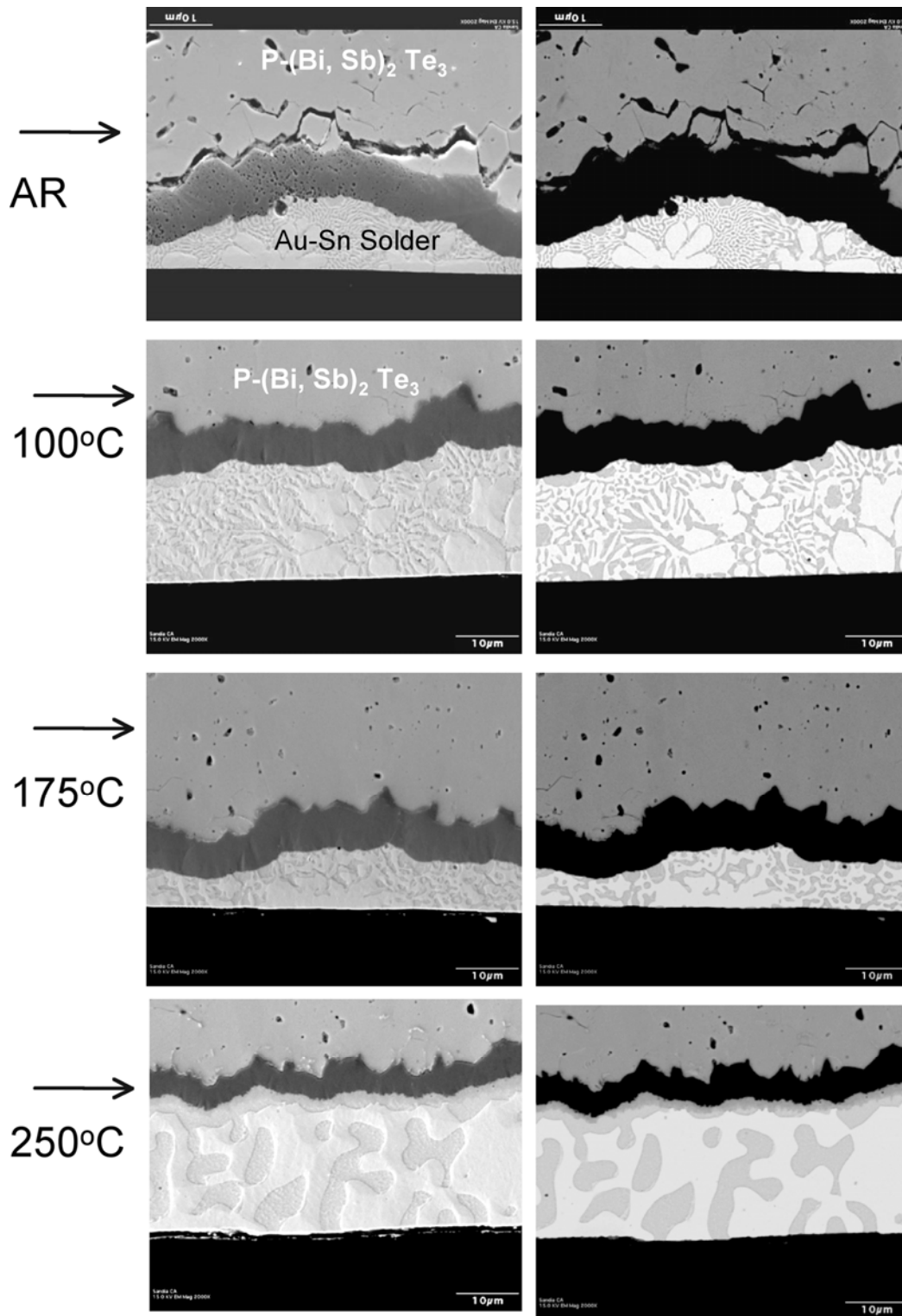


**Figure 20.** The SEI/BEI image pairs show Oswald Ripening of the lamellar Au–Sn eutectic structure. Note: the metallurgical reaction is absent in the P–(Bi, Sb)<sub>2</sub>Te<sub>3</sub> tile with Co barrier at the Au–Sn solder end.

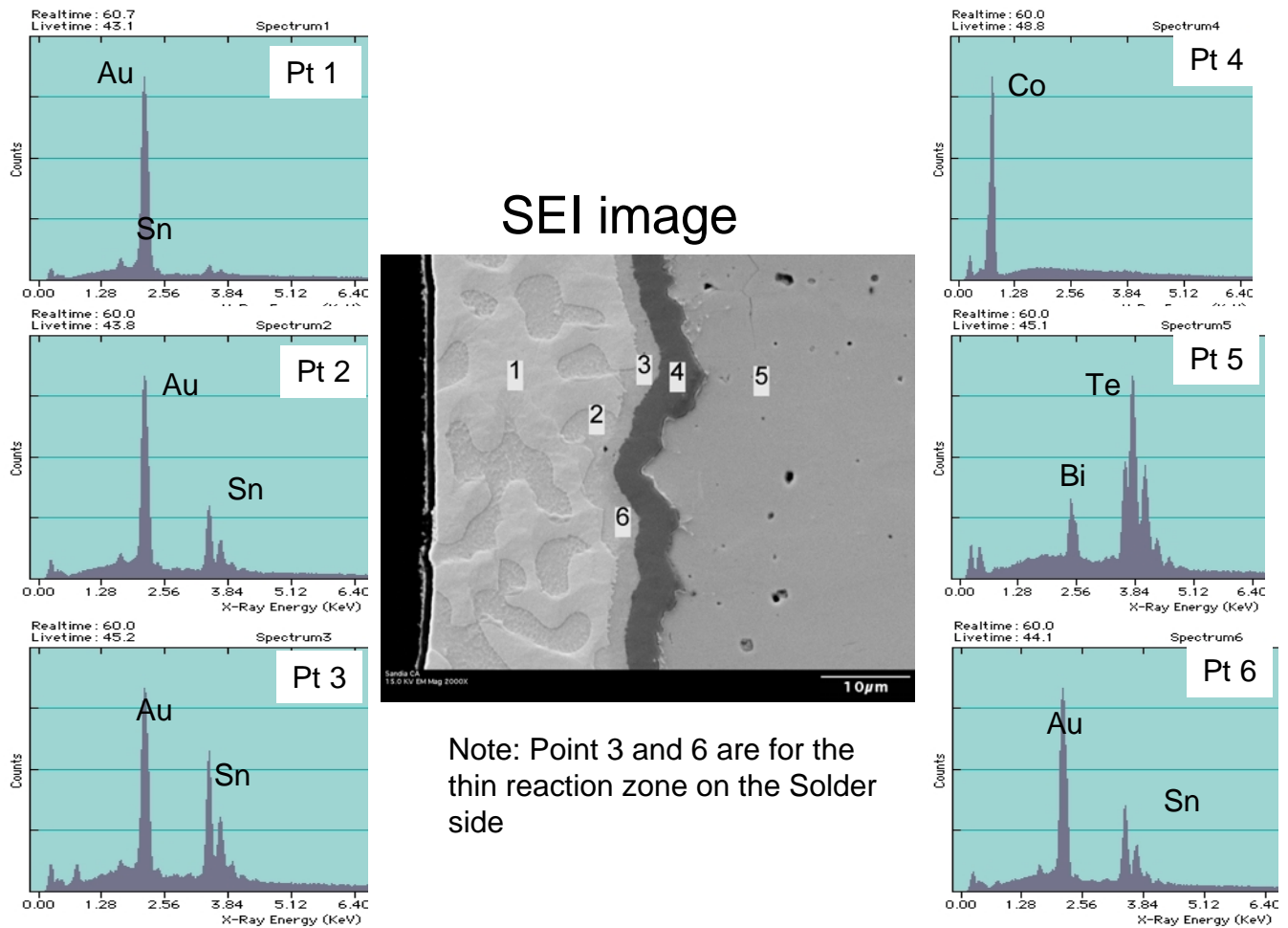


**Figure 21.** EDS spectra of each reaction feature.

**Table 7.** Semi-quantitative chemical composition (wt%) of each reaction feature by EDS.

Location	Bi	Te	Sb	Co	O	Sn	Au
Point 1	-	-	-	-	-	9.76	90.24
Point 2	-	-	-	-	-	33.86	66.14
Point 3	-	-	-	22.19	-	37.44	40.37
Point 4	-	-	-	99.98	0.02	-	-
Point 5	13.80	55.36	30.84	-	-	-	-
Point 6	-	-	-	7.81	-	38.05	54.13

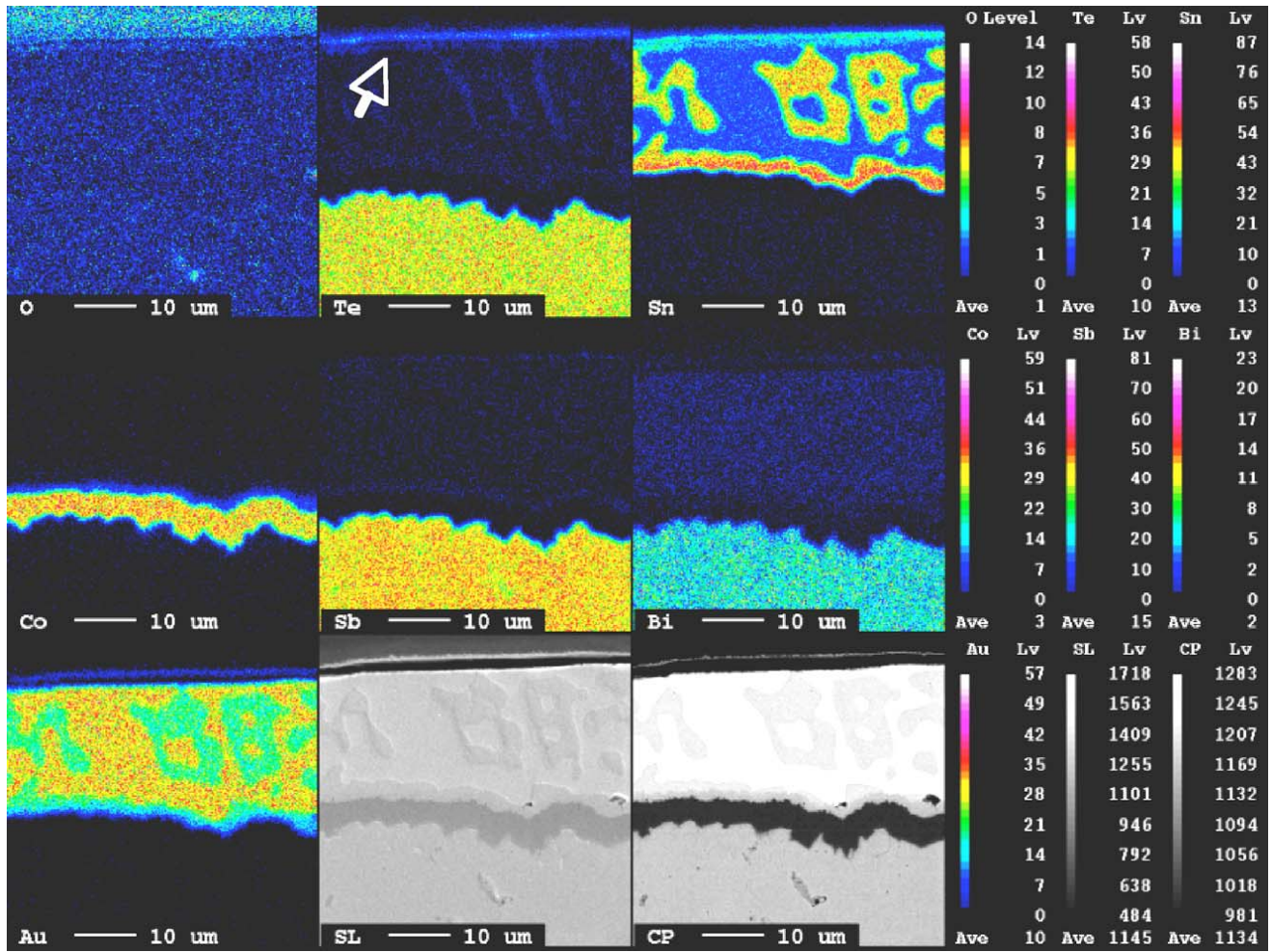


**Figure 22.** X-ray maps show the chemical enrichment for each reaction feature in the tile with a Co barrier. The corresponding SEI/BEI image pair is shown at the lower bottom.

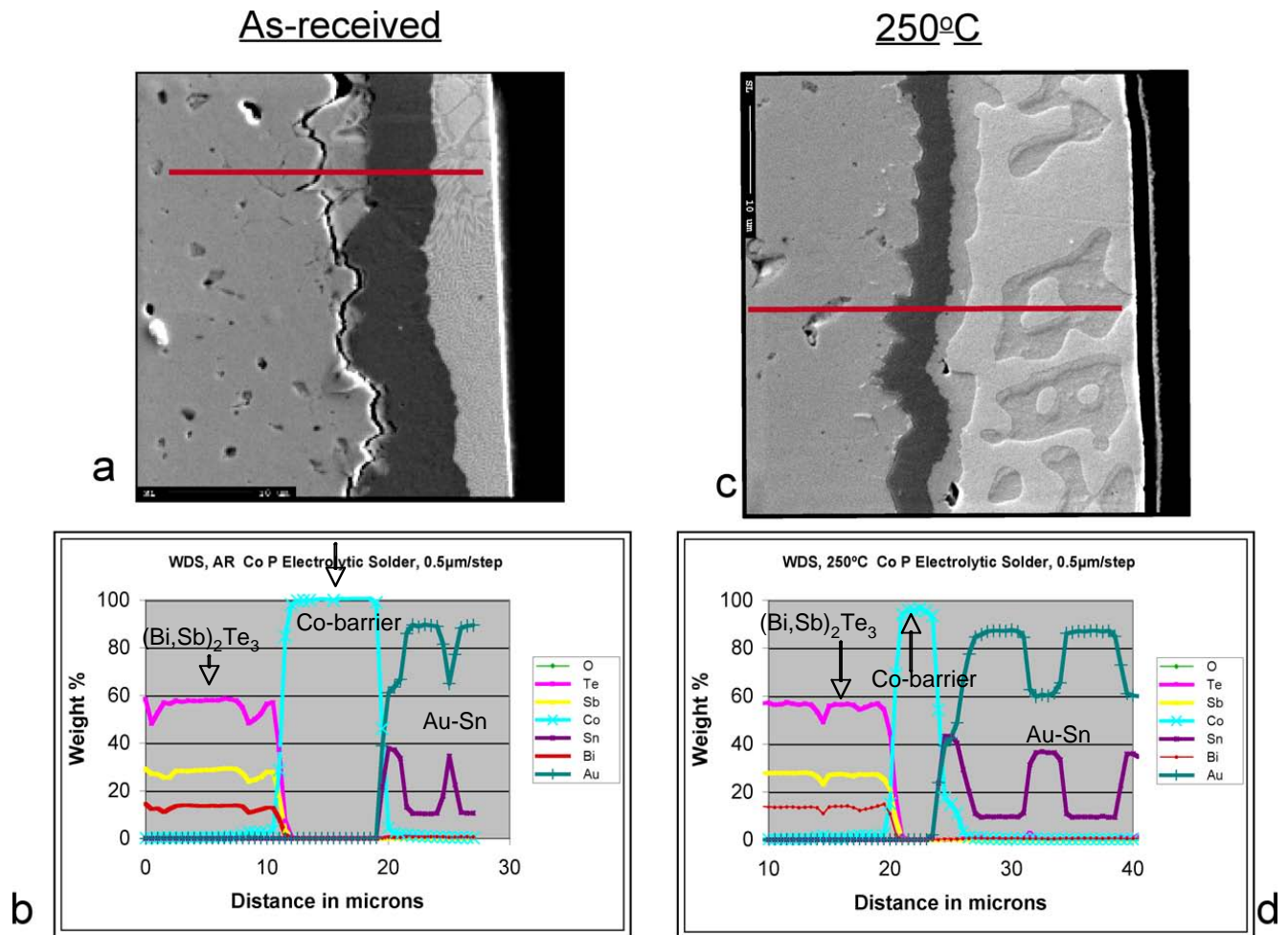


**Figure 23.** SEI images at the Co/P(Bi,Sb)<sub>2</sub>Te<sub>3</sub> interface and the WDS composition profiles across the Co/P–(Bi,Sb)<sub>2</sub>Te<sub>3</sub> interfaces; (a–b) As-received; (c–d) annealed at 250°C.

### 3.2.2.2 Co barrier on P–(Bi, Sb)<sub>2</sub>Te<sub>3</sub> tile at the Au–Sn non-soldered end

#### Metallurgical reaction between Co diffusion barrier and P–(Bi, Sb)<sub>2</sub>Te<sub>3</sub>

SEM/BEI image pairs once again show absence of the metallurgical reaction at the Co/P(Bi,Sb)<sub>2</sub>Te<sub>3</sub> interface for all annealing temperatures. This conclusion is based on the SEM/BEI image pairs, x-ray maps, and WDS composition profiles shown in Figures 24–26. The WDS composition profiles show extremely uniform composition of all the characteristic elements up to the Co/P(Bi,Sb)<sub>2</sub>Te<sub>3</sub> interface in the as-received and 250°C annealed tiles. The x-ray map again verifies the presence of Te on the surface of this Au-coated non-soldered end at  $\geq 175^\circ\text{C}$  (Figure 25 – arrows).

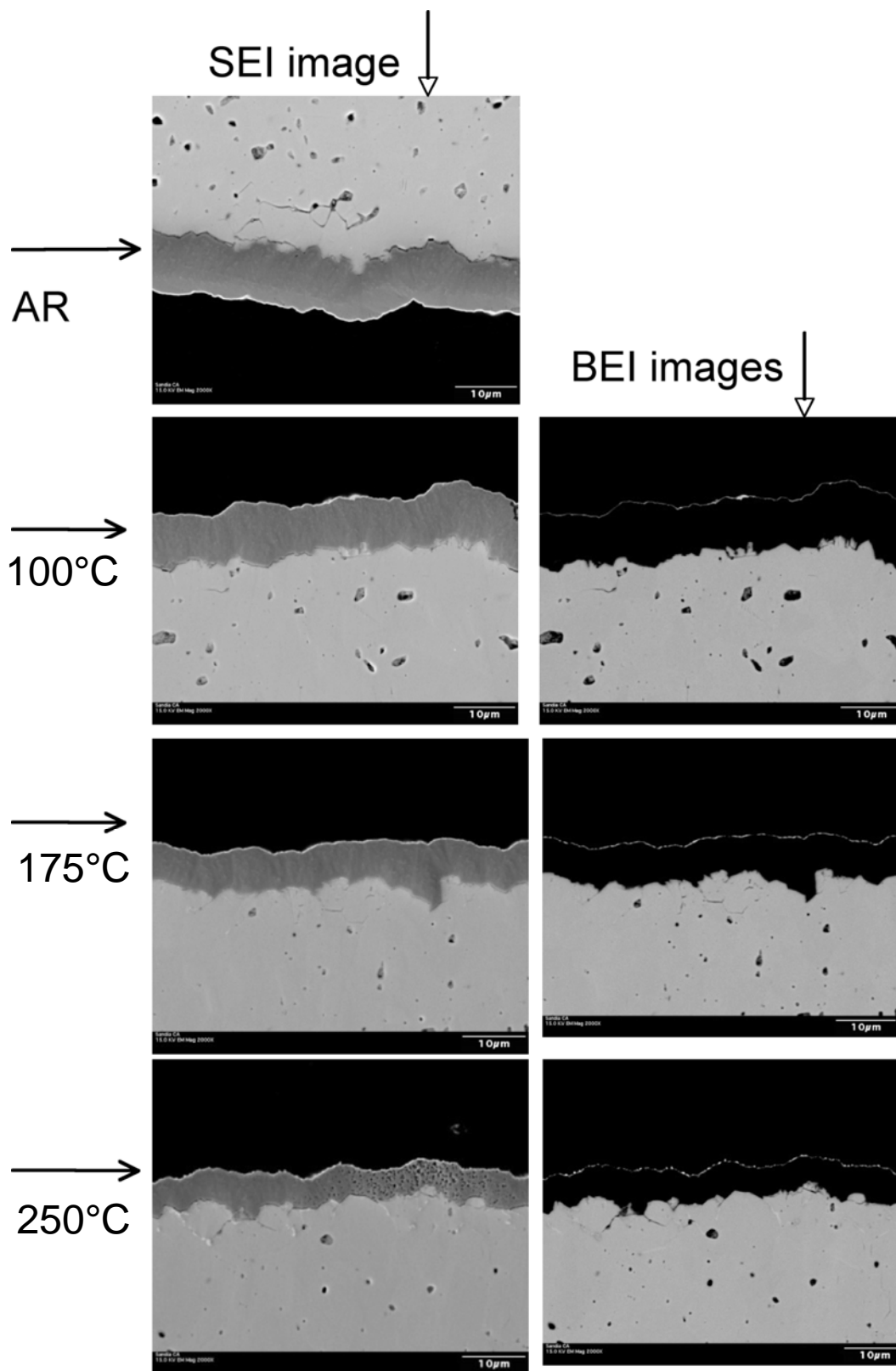


**Figure 24.** SEI and BEI images show absence of the metallurgical reaction at the Co/P-(Bi,Sb)<sub>2</sub>Te<sub>3</sub> interface.

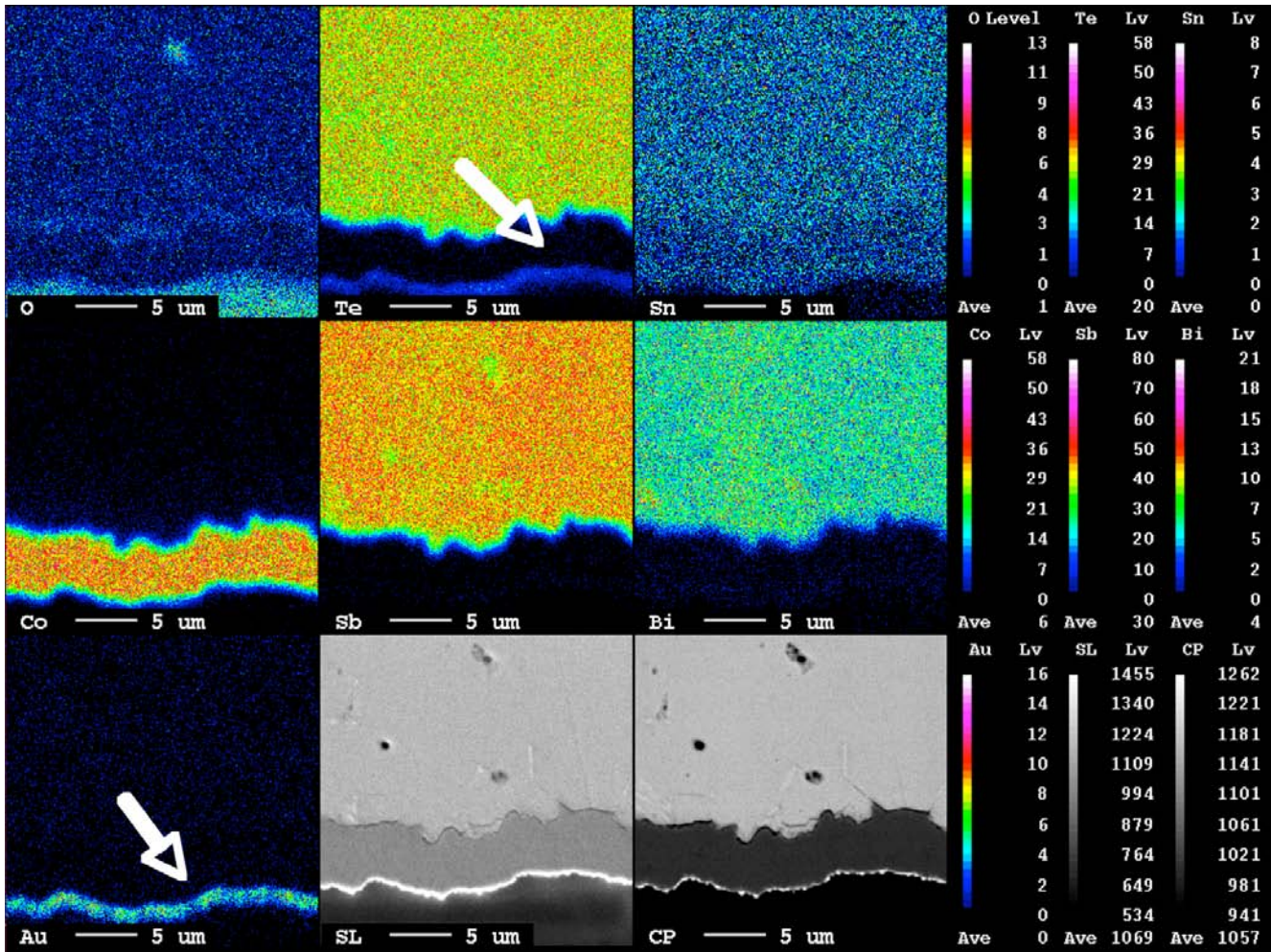


**Figure 25.** X-ray maps show absence of the metallurgical reaction and the coexistence of Te and Au on the tile surface for the tile with Co barrier at the non-soldered end.

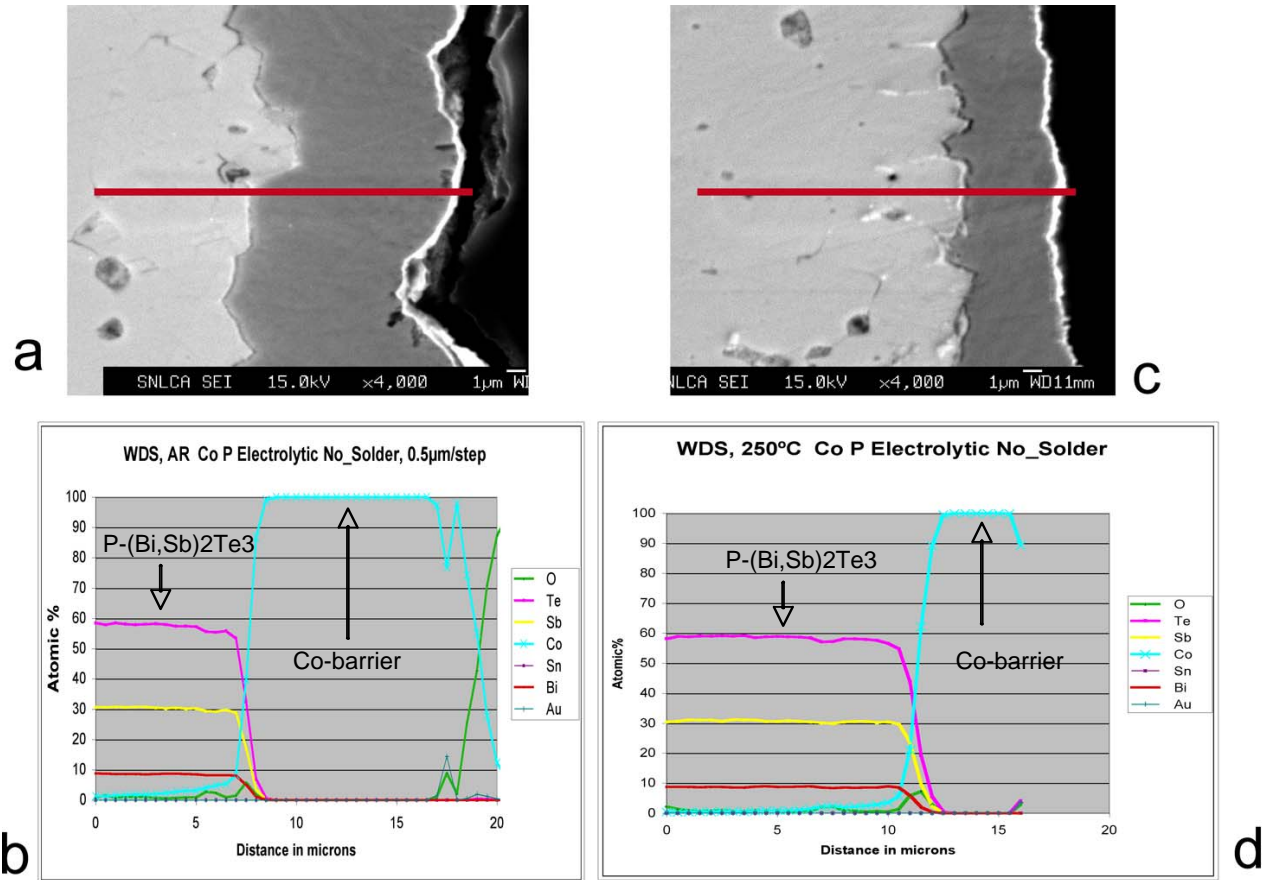


**Figure 26.** WDS composition profiles show uniform alloy composition of all the characteristic elements across the P-base alloy tight up to the Co/P(Bi,Sb)<sub>2</sub>Te<sub>3</sub> interface.

## 4. Summary and Discussions

Extensive parametric aging experiments were conducted, with temperatures ranging from ambient to 250°C and time duration from 7 to 180 days at  $10^{-4}$  torr. In addition, the metallurgical stability of P-(Bi, Sb)<sub>2</sub>Te<sub>3</sub> and N-Bi<sub>2</sub>(Te,Se)<sub>3</sub> and the interaction of P-(Bi, Sb)<sub>2</sub>Te<sub>3</sub> with Ni-phosphor and Co barriers and Au-Sn solder were examined.

This study shows that the current electroless Ni-barrier contains approximately 10 wt% phosphor rather than pure Ni. The most important finding is that the Ni-phosphor diffusion barrier appeared to be incompatible with Au-Sn solder and P-(Bi, Sb)<sub>2</sub>Te<sub>3</sub> alloy at  $\geq 175^\circ\text{C}$  in the 7day test. At the highest annealing temperature, 250°C, a similar metallurgical reaction took place to form multi-phase reaction zones on both the non-soldered and soldered ends (see Figure 27 – BEI images – left and schematic – right). This reaction led to an approximately 50% reduction in the effective thickness of the Ni-phosphor diffusion barrier. The similar microstructure and chemical evolution seen at Ni/ P-(Bi,Sb)<sub>2</sub>Te<sub>3</sub> interface between the soldered and non-soldered ends implies that the Au-Sn solder play has no role in this metallurgical reaction.

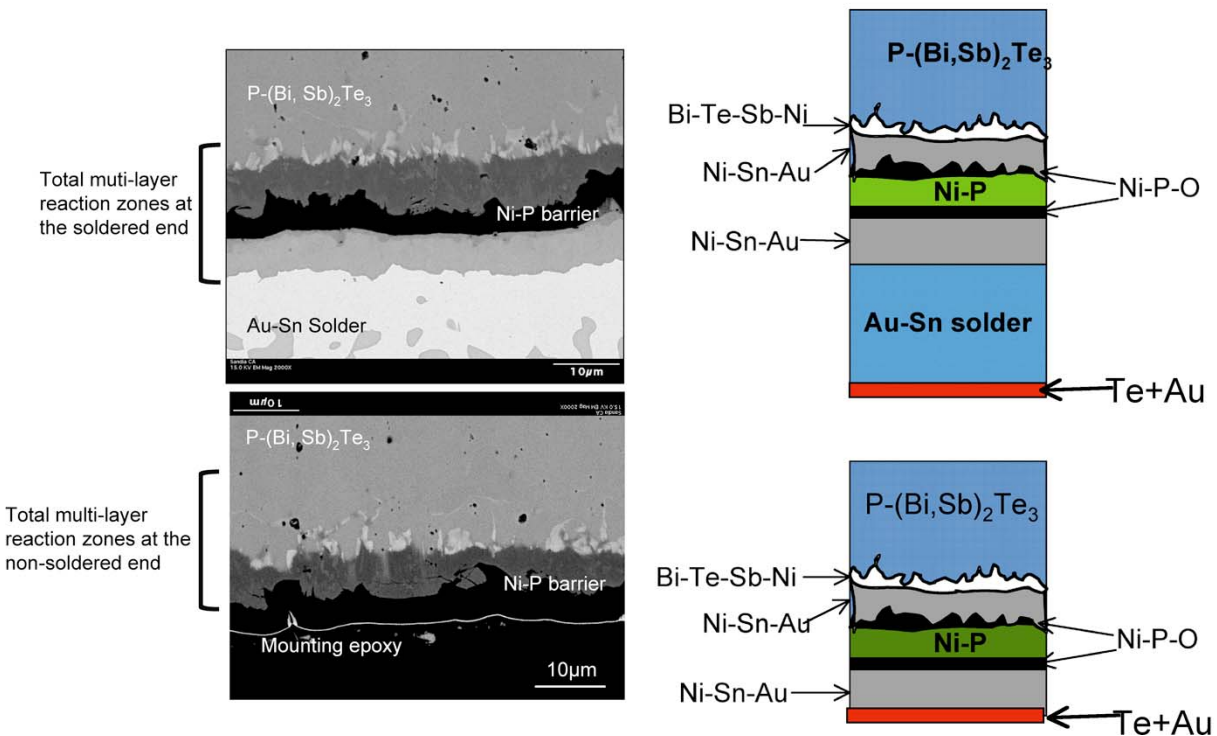


**Figure 27.** SEI/BEI images and schematics show the severe metallurgical reaction of the Ni-phosphor barrier with the P-based alloy at both the soldered and non-soldered ends.

For the tile with a cobalt barrier, the metallurgical reaction was absent at all annealing temperatures, except for a minor Co diffusion into Au–Sn solder at  $\geq 175^\circ\text{C}$  (Figure 28 – arrows). It is unclear how this minor Co diffusion could affect the integrity or long-term reliability of the interconnect assembly.

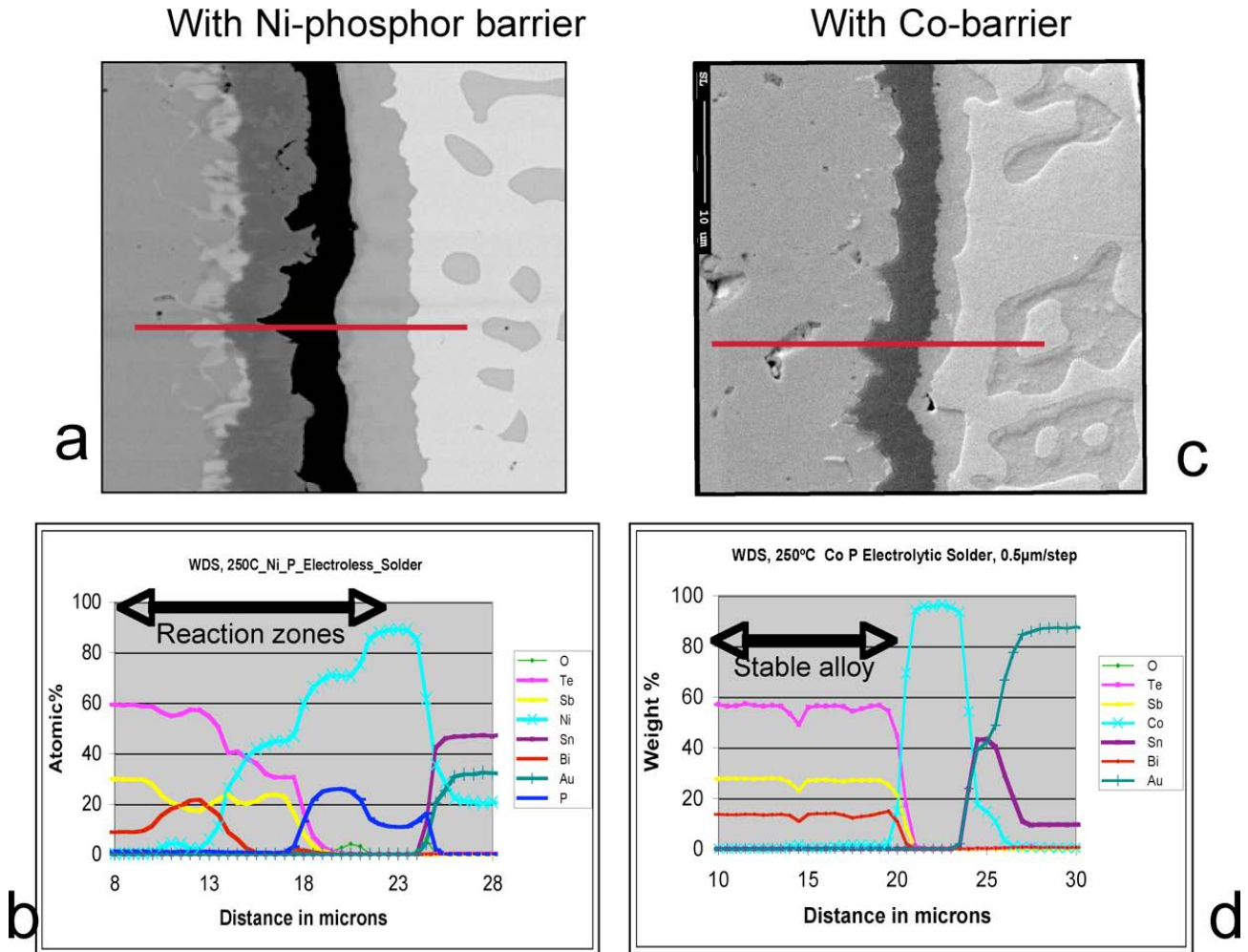


**Figure 28.** WDS composition profiles show the metallurgical reaction of the P-based alloy with Ni –phosphor, but not the Co barrier.

Another significant finding is the consistent presence of a Te-rich phase, which coexisted with the Au coating, on all tiles surfaces annealed at  $\geq 175^\circ\text{C}$  (Figure 29 – arrows). Since Te volatility is known to the TE community, it is conceivable that the Te-rich phase is a result of Te-vapor condensation and a subsequent Te–Au surface reaction. It is unclear how the Te-loss, due to thermal annealing, would affect the required P–(Bi,Sb)<sub>2</sub>Te<sub>3</sub> stoichiometry in the long run.

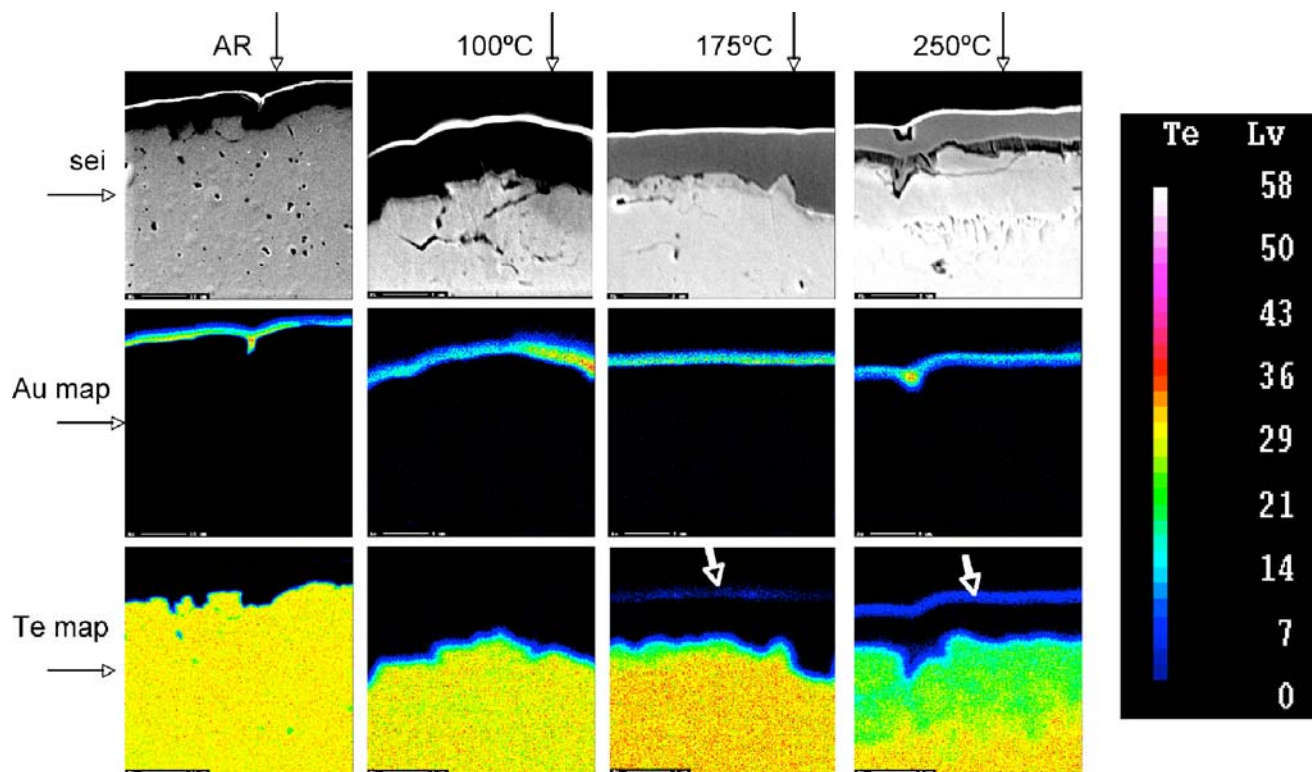


**Figure 29.** Te and Au x-ray maps show the coexistence of Te and Au on the tile at the non-soldered end.

## 5. Conclusions

- The current Ni–phosphor diffusion barrier is incompatible with P–(Bi,Sb)<sub>2</sub>Te<sub>3</sub> or Au–Sn solder at temperatures  $\geq 175^\circ\text{C}$ , due to the metallurgical reactions starting at the Ni/P(Bi,Sb)<sub>2</sub>Te<sub>3</sub>/Au–Sn interfaces. The Ni–phosphor is therefore not suitable for SNL’s elevated temperature ( $\geq 175^\circ\text{C}$ ) use.
- The electrolytic Co barrier appeared to be compatible with P(Bi,Sb)<sub>2</sub>Te<sub>3</sub> at all annealing temperatures. Metallurgical reaction is absent at the Co/P(Bi,Sb)<sub>2</sub>Te<sub>3</sub> interface, with the exception of a minor Co diffusion into Au–Sn solder. However, the minor effect of the Co/Au–Sn interaction on TE system reliability and long-term ( $\gg 7$ days) thermal stability of Co barrier has yet to be determined.
- Tellurium volatility from the P–(Bi,Sb)<sub>2</sub>Te<sub>3</sub> was evident at temperatures  $\geq 175^\circ\text{C}$ , regardless of the type of diffusion barrier used. The Te evaporation rate needs to be assessed in order to determine how long the P–(Bi,Sb)<sub>2</sub>Te<sub>3</sub> could maintain its required stoichiometry.

## **6. Future Work**

The current document is a progress report, covering only the P-type alloy with Ni and Co barrier tiles over 7-days aging. Currently, the material characterization activities are continuing for the remaining N-type tiles with 7-days aging, as shown in Table 8. In addition, the thermal aging experiments for the 72 samples of 90-days and 180-days aging are ongoing, and the material characterization will proceed upon the completion of the experiment in FY09–FY10.

**Table 8.** Samples to be characterized in FY09–FY10.

Sample ID	Au-Sn Solder	Temp.(oC)	P-type	N-type
Ni (Electroless)	Solder end	AR	X	X
		100uC	X	X
		175uC	X	X
		250uC	X	X
	Non-solder end	AR	X	X
		100uC	X	X
		175uC	X	X
		250uC	X	X
Co (Electrolytic)	Solder end	AR	X	X
		100uC	X	X
		175uC	X	X
		250uC	X	X
	Non-solder end	AR	X	X
		100uC	X	X
		175uC	X	X
		250uC	X	X
Co (electroless)	Solder end	AR	Material characterization aborted due to incorrect diffusion barrier chemical composition, i.e. Ni-Co alloy	
		100uC		
		175uC		
		250uC		
	Non-solder end	AR		
		100uC		
		175uC		
		250uC		
Pd (Electrolytic)	Solder end	<b>N/A</b>		
	Non-solder end	AR	X	X
		100uC	X	X
		175uC	X	X
		250uC	X	X
Pd (Electroless)	Solder end	<b>N/A</b>		
	Non-solder end	AR	X	X
		100uC	X	X
		175uC	X	X
		250uC	X	X

## References

1. “Metallurgy, thermal stability and failure mode of the commercial Bi–Te- based TE modules,” Nancy Yang and A. Morales, SAND report, SAND2009-0758, 2009.
2. “Interface Characterization of Nickel contacts to bulk bismuth tellurium selenide,” D. Lyore, etc. *Wiley Interscience* 3, March 2009.
3. “Effect of interfacial compound formation on contact resistance of solder junctions between Bismuth Telluride-based thermoelements and copper,” Chien–Neng Liao, C. H. Lee, W. J. Chen, *Electrochemical and Solid State Letters*, 10(9) p. 23–25, 2007.

# Distribution

## Various people...

2	9018	Central Technical Files	8944
1	0899	Technical Library	4536

Glenn Kubiak, 8600  
Bill Even, 8650  
Sarah Allendorf, 8656  
Doug Medlin, 8656  
Nancy Yang, 8651 (15)  
Andy Gardea, 8651  
Jeff Chames, 8651  
Miles Clift, 8651  
Ryan Nishimoto, 8651  
April Nissen, 8223  
Davina Kwon, 8220  
Thomas Felter, 8222  
Tim Shepodd, 8223  
Paul Spence, 8224  
Peter Van Blarigan, 8224  
Andrew Shugard, 8224  
Alfredo Morales, 8223  
Scott Whalen, 2547  
Manuel Contreras 2547  
Steve Rice, 8224  
Bob Oetken, 8244  
Doug Gehmlich, 8200  
Chris Apblett, 1815  
Daniel Wesoloski, 2547  
Rion Causey, 8651  
Dorian Balch, 8224  
Jim Handrock, 8200  
Mike Chiesa, 8246  
Thomas Felter, 8222  
Richard Salzbrenner, 1820